



**FEDERAL UNIVERSITY OF ITAJUBÁ**

**EDSON DA COSTA BORTONI**

**EFFICIENCY MAP AND WEIGHTED AVERAGE EFFICIENCY FOR SYNCHRONOUS  
MACHINES FOR HYDROPOWER PLANTS**

Thesis presented to the board selected by the Electric and Energy Systems Institute (ISEE) of the Federal University of Itajubá (UNIFEI), as part of Full Professor grade elevation.

July 2019  
Itajubá

To my wife Cristina, and daughters Beatriz and Luiza. You have allowed me wonderful times!  
Thank you very much!

## ACKNOWLEDGMENT

First of all, I would like to praise God presented in his full expression: Father, Son, and Holy Spirit, for the grace of communion, the grace to live in grace, the grace to have my natural family devoted to him, and the grace for giving me eternal life. I also recognize my working friends at EXCEN, professors Jamil Haddad, Luiz Augusto Horta Nogueira, Roberto Akira Yamachita, and Marcos Dias. I appreciate my students, represented by José Vitor Berndardes Jr. and Bruno Tonsic Araujo for what they have been doing in turning crazy ideas into real things. I also appreciate my former students, represented by Roberto T. Siniscalchi and Marco Aurélio Siqueira Mauro, who supply real data in order to test new developments. I express my gratitude to professors of other institutes, hereby represented by Prof. Roberto Alves de Almeida and Prof. Luiz Eduardo Borges da Silva. I express many thanks to retired professors, represented by Prof. Augusto Nelson Carvalho Viana and Prof. Germano Lambert Torres. Many thanks to the colleagues from the industry in which I have learned a lot on how to effectively construct the things that we use to view in theory, hereby represented by Johnny Rocha and Mauro Uemori. I cannot pass up the opportunity to specifically acknowledge professors Zulcy de Souza and Antônio Eduardo Hermeto as references to my daily and academic life. I also would like to recognize all of my colleagues from the IEEE PES Task Force on Grid Code Impacts on Generator Standards for the initial ideas, and the Energy Department of the Politecnico di Torino, who have provided me a friendly environment to the development of this thesis. A special thanks to the professors Andrea Cavagnino, Alberto Tenconi, Silvio Vaschetto, and Carlo Ragusa, and the precious help in Matlab coding received from the doctoral student Simone Ferrari.

## ABSTRACT

In recent years there has been a claim of evaluating the weighted average efficiency of synchronous machines for hydro-generation application instead of a single value at the rated condition in order to consider the most frequent loadings. This work contributes to mapping the efficiency of a synchronous machine limited by its capability chart. In a second opportunity, a histogram of an operating generator is obtained. The crossing of the aforementioned information allows for the obtaining of a weighted average efficiency in full capable operation. Some aspects that lead the machine to operate out from the rated point are raised along with the efficiency-oriented design issues. The theory involving losses and capability chart of the machine is presented. The behavior of the losses in loadings different than the rated one is presented as well in which a theoretical model is included to achieve the efficiency of any loading by using the rated load efficiency obtained by an approach of an infrared-based calorimetric test. The proposed methodology is applied to the existent machine.

Key words: Synchronous machines, weighted average efficiency, machine design, theoretical evaluation, field test.

## LIST OF FIGURES

FIGURE 1.1. TOTAL SOLAR INSTALLED CAPACITY BY REGION [1] .....	1
FIGURE 1.2. WORLDWIDE WIND POWER INSTALLED CAPACITY [3].....	2
FIGURE 1.3. WORLDWIDE OFFSHORE WIND POWER INSTALLED CAPACITY 2017 [1.2].....	3
FIGURE 1.4. MARKET SHARE OF TOP 10 TURBINE MANUFACTURERS [1.2].....	3
FIGURE 1.5. POSITIONING OF ENERGY STORAGE TECHNOLOGIES [1.12] .....	4
FIGURE 1.6. WORLD INSTALLED HYDROPOWER CAPACITY AT THE END OF 2016 [1.12] .....	5
FIGURE 1.7. HYDROPOWER CAPACITY AND GENERATION BY REGION [1.12] .....	5
FIGURE 2.1. WIND VARIATION OVER ONE YEAR [2.1] .....	8
FIGURE 2.2. SOLAR POWER OVER ONE YEAR [2.1] .....	8
FIGURE 2.3. INFLOW VARIATION OF TWO DIFFERENT POWER PLANTS .....	9
FIGURE 2.4. GROSS HEAD VARIATION OVER TIME .....	11
FIGURE 2.5. GROSS HEAD VARIATION DURATION CURVE .....	11
FIGURE 2.6. OPERATION CHART OF HYDROTURBINE.....	12
FIGURE 2.7. DIMENSIONAL ANALYSIS OF A GENERATOR .....	13
FIGURE 2.8. LOSSES PARTICIPATION IN THE TOTAL LOSS .....	17
FIGURE 2.9. PERCENTAGE MAGNITUDE LOSSES VARIATION .....	18
FIGURE 2.10. MACHINES CROSS-SECTIONS .....	18
FIGURE 2.11. EFFICIENCY CONTOUR, CONSIDERING LOADING AND WEIGHTS .....	21
FIGURE 3.1. POWER FLOW CONSIDERING EXCITATION POWER .....	23
FIGURE 3.2. POTIER DIAGRAM FOR A CYLINDRICAL ROTOR SYNCHRONOUS MACHINE .....	27
FIGURE 3.3. STRAY-LOAD LOSS VARIATION [3.1] .....	28
FIGURE 3.4. CORE LOSS VARIATION [3.1] .....	28
FIGURE 4.1. IR THERMAL IMAGE OF A GENERATORS IN A POWER PLANT .....	31
FIGURE 4.2. CONTROL VOLUME AROUND THE ELECTRICAL MACHINE .....	32
FIGURE 4.3. COMBINED BEARING HEAT EXCHANGER (A) AND THERMAL IMAGE (B) .....	33
FIGURE 4.4. IR THERMAL IMAGES FROM THE MACHINE OIL COOLED BEARINGS .....	33
FIGURE 4.5. CAMERA FOV AND COVERED AREA .....	38
FIGURE 4.6. IR THERMAL IMAGE AND ISOTHERM OF COVERING SURFACE .....	39
FIGURE 4.7. IR THERMAL IMAGE OF A GENERATOR SHAFT .....	40
FIGURE 5.1. PHASOR DIAGRAM .....	42
FIGURE 5.2. ELECTRIC DIAGRAM .....	43
FIGURE 5.3. PHASOR DIAGRAM .....	43
FIGURE 5.4. PHASOR DIAGRAM FOR ROUNDED ROTOR SYNCHRONOUS MACHINES .....	44
FIGURE 5.5. PHASOR DIAGRAM FOR SALIENT POLE SYNCHRONOUS MACHINES.....	45
FIGURE 5.6. P-Δ DIAGRAM FOR A ROUND ROTOR SYNCHRONOUS MACHINE .....	46
FIGURE 5.7. P-Δ DIAGRAM FOR A SALIENT POLE SYNCHRONOUS MACHINE .....	47
FIGURE 5.8. CAPABILITY CHART FOR A SALIENT POLE SYNCHRONOUS MACHINE .....	48
FIGURE 5.9. CAPABILITY CHART FOR A ROUNDED ROTOR SYNCHRONOUS MACHINE .....	48
FIGURE 5.10. MODIFIED PHASOR DIAGRAM .....	49
FIGURE 5.11. LIMITS OF A CAPABILITY CHART FOR A ROUNDED ROTOR MACHINE .....	50
FIGURE 5.12. OPERATION UNDER FLUX WEAKNESS CONDITION.....	50
FIGURE 5.13. V-CURVE AND ARMATURE CORE-END HEATING LIMITS CONSTRUCTION .....	51
FIGURE 5.14. REDUCTION OF EFFECTS OF TRANSVERSAL FLUXES .....	51

FIGURE 5.15. PHASOR DIAGRAM FOR SALIENT POLE SYNCHRONOUS MACHINE .....	52
FIGURE 5.16. INTRODUCTION OF LIMITS .....	52
FIGURE 5.17. OPERATING LIMITS OF A SALIENT-POLE SYNCHRONOUS MACHINE .....	54
FIGURE 5.18. CAPABILITY CURVE OF A SALIENT-POLE SYNCHRONOUS MACHINE .....	55
FIGURE 6.1. COMPLETE PER-UNIT SATURATION CURVE .....	61
FIGURE 6.2. V-CURVE FAMILY FOR THE MACHINE UNDER TEST .....	62
FIGURE 6.3. EFFICIENCY MAP OF THE TESTED MACHINE .....	63
FIGURE 6.4. EFFICIENCY MAP LIMITED BY ITS CAPABILITY CHART .....	64
FIGURE 6.5. HISTOGRAM OF THE LOADING IN 2017 .....	65
FIGURE 6.6. LOADING IN 2017 .....	66
FIGURE 6.7. 2D-HISTOGRAM OF THE LOADING IN 2017 IN THE P-Q PLANE .....	67
FIGURE 6.8. 2D-HISTOGRAM WITH EMPHASIS IN THE HIGH ACTIVE POWER .....	68

## LIST OF TABLES

TABLE 2.1. RATED QUANTITIES OF THE STUDIED MACHINES .....	15
TABLE 2.2. FUNDAMENTAL QUANTITIES BEHAVIOR .....	16
TABLE 2.3. LOSSES BEHAVIOR .....	16
TABLE 2.4. TOTAL LOSSES AND EFFICIENCY BEHAVIOR .....	16
TABLE 4.1. TYPICAL CONSTANT VALUES (@ 300K) .....	33
TABLE 4.2. TYPICAL VALUES OF A AND B .....	35
TABLE 5.1. REGULATOR FUNCTIONS .....	45
TABLE 6.1. LOSS IN THE RADIATOR .....	56
TABLE 6.2. LOSS IN THE SURFACES .....	56
TABLE 6.3. AMBIENT QUANTITIES .....	57
TABLE 6.4. LOSS IN THE RADIATOR .....	57
TABLE 6.5. LOSS IN THE SURFACES .....	57
TABLE 6.6. AMBIENT QUANTITIES.....	58
TABLE 6.7. LOSS IN THE RADIATOR .....	58
TABLE 6.8. LOSS IN THE SURFACES .....	58
TABLE 6.9. AMBIENT QUANTITIES.....	58
TABLE 6.10. FULL LOAD LOSSES .....	59
TABLE 6.11. AMBIENT QUANTITIES.....	59
TABLE 6.12. QUANTITIES FOR THE BEARING LOSS CALCULATION .....	60
TABLE 6.13. RESULTS OBTAINED IN THE NO-LOAD SATURATION TEST. ....	60
TABLE 6.14. CHARACTERISTICS OF THE NO-LOAD SATURATION DATA .....	60
TABLE 6.15. COEFFICIENTS OF THE PER-UNIT NO-LOAD SATURATION FUNCTION.....	61

## SUMMARY

DEDICATION .....	ii
ACKNOWLEDGMENT .....	iii
ABSTRACT .....	iv
LIST OF FIGURES .....	v
LIST OF TABLES .....	vii
SUMMARY .....	viii
1. INTRODUCTION .....	1
2. THE WEIGHTED AVERAGE EFFICIENCY CONCEPT.....	7
2.1. THE OPERATION OUT FROM RATED CONDITIONS .....	7
2.1.1. THE INFLUENCE OF NEW RENEWABLES .....	7
2.1.2. ENERGETIC ISSUES .....	9
2.1.3. ELECTRICITY MARKET ISSUES .....	12
2.2. EFFICIENCY ORIENTED DESIGN .....	13
2.3. WEIGHTED AVERAGE EFFICIENCY.....	19
3. MACHINE LOSSES AND EFFICIENCY .....	22
3.1 EFFICIENCY AND LOSSES DEFINITIONS.....	22
3.2 THE DIVERSE NATURE OF THE LOSSES.....	22
3.2.1. CURRENT LOSSES IN THE ARMATURE ( $P_{SC}$ ) .....	22
3.2.2. CURRENT LOSSES IN THE ROTOR ( $P_{RC}$ ) .....	23
3.2.3. STATOR CORE LOSSES ( $P_C$ ).....	23
3.2.4. STRAY-LOAD LOSSES ( $P_S$ ).....	23
3.2.5. WINDAGE LOSSES ( $P_W$ ) .....	23
3.2.6. EXCITATION LOSSES ( $P_E$ ) .....	23
3.2.7. BUSH LOSSES ( $P_{br}$ ) .....	24
3.2.8. BEARING LOSSES ( $P_B$ ) .....	25
3.3 DETERMINATION OF THE LOSSES FOR ANY LOADING CONDITION .....	25
3.3.1 CONSTANT LOSSES .....	25
3.3.2 ARMATURE CURRENT-DEPENDENT LOSSES.....	25
3.3.3 FIELD CURRENT-DEPENDENT LOSSES.....	26
3.4. LOSSES AND EFFICIENCY CALCULATION FOR ANY LOAD .....	28
3.5. EFFICIENCY CALCULATION .....	29
4. INFRARED BASED CALORIMETRIC METHOD .....	30
4.1 THE CALORIMETRIC METHOD.....	31
4.2 THE CALORIMETRIC METHOD USING IR THERMAL IMAGING .....	32
4.2.1 LOSSES ABSORBED BY COOLANT FLUIDS.....	32
4.2.2 LOSSES RELEASED BY RADIATION, CONVECTION, AND CONDUCTION .....	34
4.2.3 HEAT TRANSFER COEFFICIENT.....	34
4.2.4 TEMPERATURE MEASUREMENT.....	36
4.2.4.1 FOV SPAN.....	37
4.2.4.2 ISOTHERM DIAGRAMS .....	38
4.2.4.3 LOSS IN THE MACHINE SHAFT .....	39
4.3 LOSS SEGREGATION .....	40

4.3.1 FIRST RUNNING .....	40
4.3.2 SECOND RUNNING .....	41
4.3.1 THIRD RUNNING .....	41
5. CAPABILITY CHART OF A GENERATOR.....	42
5.1 PHASOR DIAGRAM .....	42
5.2 STEADY STATE OPERATION .....	45
5.3 P-Δ DIAGRAM .....	46
5.4 CAPABILITY CHART .....	47
5.4.1 CAPABILITY CONSTRUCTION.....	49
6 VALIDATION AND APPLICATION TO EXISTENT MACHINES .....	56
6.1 TESTS FOR LOSSES EVALUATION .....	56
6.1.1. FIRST RUNNING .....	56
6.1.2. SECOND RUNNING .....	57
6.1.3. THIRD RUNNING .....	58
6.1.4. TESTS AT FULL LOAD.....	59
6.2 NO-LOAD SATURATION FUNCTION TEST.....	60
6.3 LOSSES AND EFFICIENCY CALCULATION FOR ANY LOAD .....	62
7 CONCLUSIONS.....	70
BIBLIOGRAPHICAL REFERENCES.....	71

## CHAPTER 1

### INTRODUCTION

With the worldwide increase in consumption of electricity and the use of exhaustible resources, new forms of power generation have been developed along with the reduction of environmental impact. New renewable power generation based on wind, sun, hydro, oceanic, and geothermal potentials, among others, have been proposed and implemented. Solar, wind and hydro compositions are the most significant alternatives and make up this introduction.

In many countries, the use of renewable energy has been growing exponentially since the end of the last decade. By the end of 2017, the total worldwide installed capacity of photovoltaic was 402 GW. China lead the photovoltaic generation capacity of 131.1 GW, followed by United States (USA) with 51.5 GW, Japan with 49.8 GW and Germany with 43 GW as shown in Fig. 1.1 [1.1]. According to data from the Brazilian Ministry of Mines and Energy, Brazil was among the thirty countries with an installed capacity higher than 1 GW at the end of 2017, putting it among the top ten countries that most add more PV plants to the Brazilian energy mix [1.2].

Brazilian solar potential is higher when compared to other countries; the northeast region presents the most significant values of global solar irradiance. In addition, this area provides favorable climate conditions throughout the entire year. The average Brazilian irradiance is between 1,200 and 2,400 kWh/m<sup>2</sup>year, which is greater than average European values [1.2].

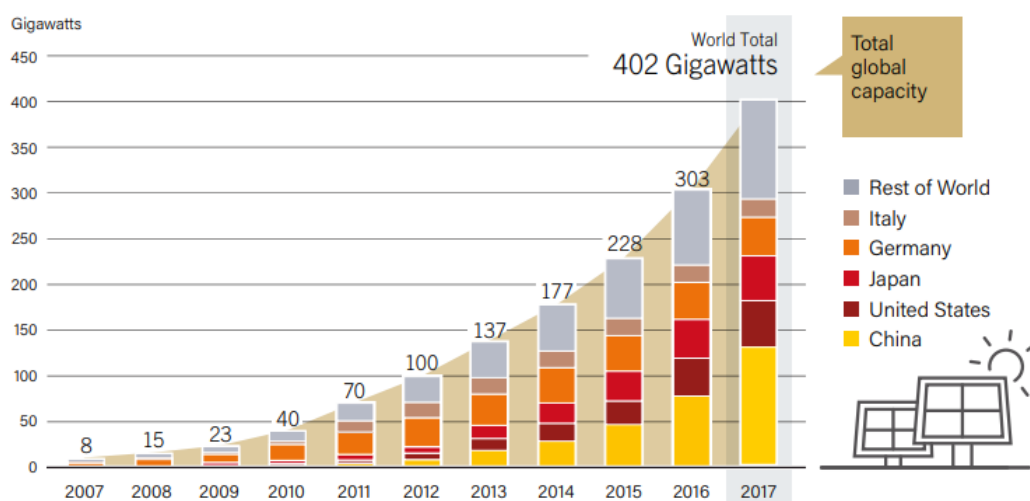


Figure 1.1. Total solar installed capacity and contribution by region [1].

Wind generation has been gaining considerable attention worldwide due to its appeal in the context of renewable energy generation [1.3]. In 2017, the worldwide installed capacity of wind generation was more than 500 GW as shown in Fig. 1.2. The main areas of the world contributors of this installed power were Asia, Europe, North America, Latin America, Africa and the Middle East. China, the United States, and Germany are the countries with the most participation in this installed capacity with respective percentages of 34.9%, 16.5%, and 10.4% [1.3].

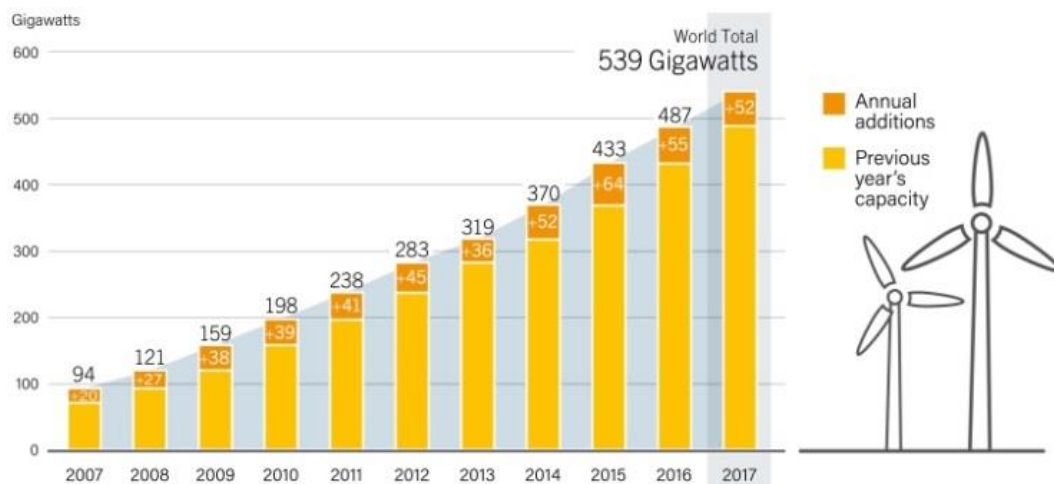


Figure 1.2. Worldwide wind power installed capacity [3].

Whilst worldwide governments have reduced, or even eradicated, tax incentives, off-shore production has shown a bigger increase than on-shore solutions, moving beyond the planning process as shown in Fig. 1.3 [1.4]. The main technical reasons regard the flatness and smaller roughness of the surface in addition to high wind speeds with smaller variations, leading to higher power density than on-shore generation. Leveled-off long-term costs have also proven to be smaller among off-shore projects than in on-shore [1.4]-[1.5].

On the other hand, there are several technologies related to electric machinery offered by the main manufacturers as shown in Fig. 1.4. The choosing dilemma is not limited to the decision of whether a synchronous or an asynchronous generator must be used, but rather if a speed amplifier must be used or not in order to obtain smaller electric machines. The size of power electronics and harmonics are also issues that must be analyzed [1.6]-[1.8].

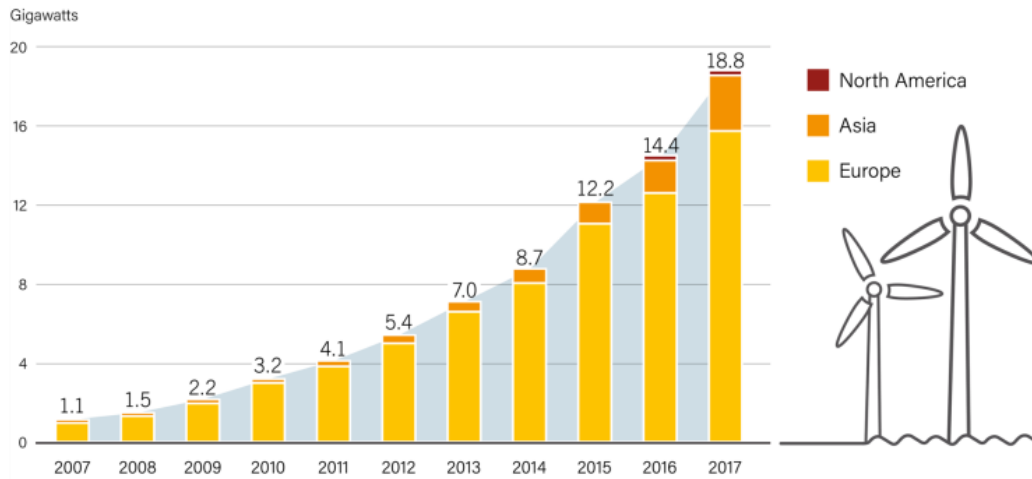


Figure 1.3. Worldwide offshore wind power installed capacity 2017 [1.2].

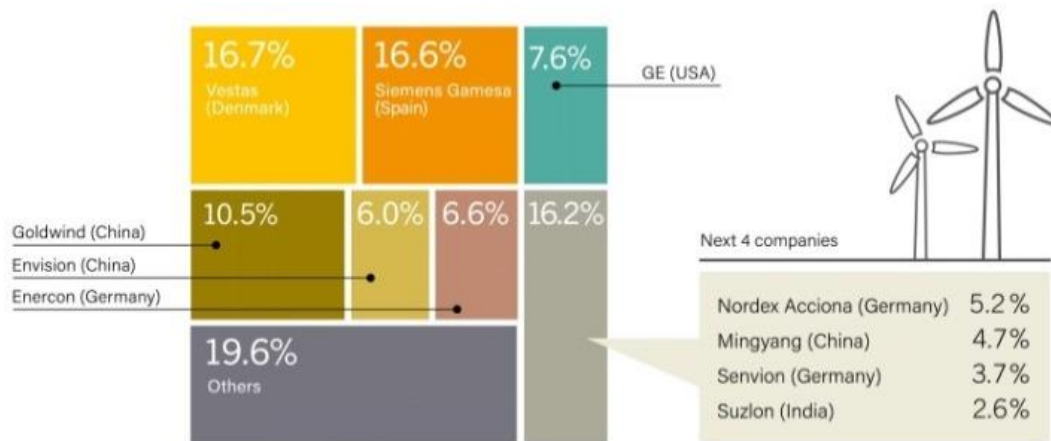


Figure 1.4. Market Share of Top 10 Turbine Manufacturers [1.2].

The production of electricity from sustainable resources has shown astounding development worldwide. Likewise, new loads on the power system network have been done without a proper increase of sources that can be dispatched. This fact implies a possible system instability since the availability is dependent on renewable intermittent. In turn, the use of energy storage systems (ESS) and renewable sources becomes indispensable for generation operation and control [1.9].

As long as alternate current electricity cannot be stored, it must be converted into another type of energy, such as kinetic, electrochemical, or potential energy, in order for it to be stored. Such storage allows for electricity to be dispatched in periods of both high demand and low generation, thus acting as a backup in cases where the main generation becomes inaccessible [1.10]. In addition, it helps to reduce the usage of exhaustible fossil fuels while cutting down on greenhouse gas emissions associated with global warming.

The ESS has attracted the attention of governments, investors, stakeholders, and researchers as it aims to improve the reliability and resilience of the overall energy supply chain [1.10]. The functionality of micro-networks and smart grids shows the new deployed storage power capacity across global markets for the year 2017 [1.11].

The increased penetration of distributed generation (DG) on the grid impacts the system. For example, on a PV farm on a cloudy day, the produced generation goes down and as a consequence, the voltage delivered to the load is reduced. In other words, the system will present faster voltage variations. In order to reduce this contingency, an ESS can be used. Figure 1.5 illustrates the characteristics of various ESS options in terms of system power rating and discharge time. Among these technologies, a battery energy storage system (BESS) is the most attractive due to its technological maturity and ability to provide both sufficient energy and power densities.

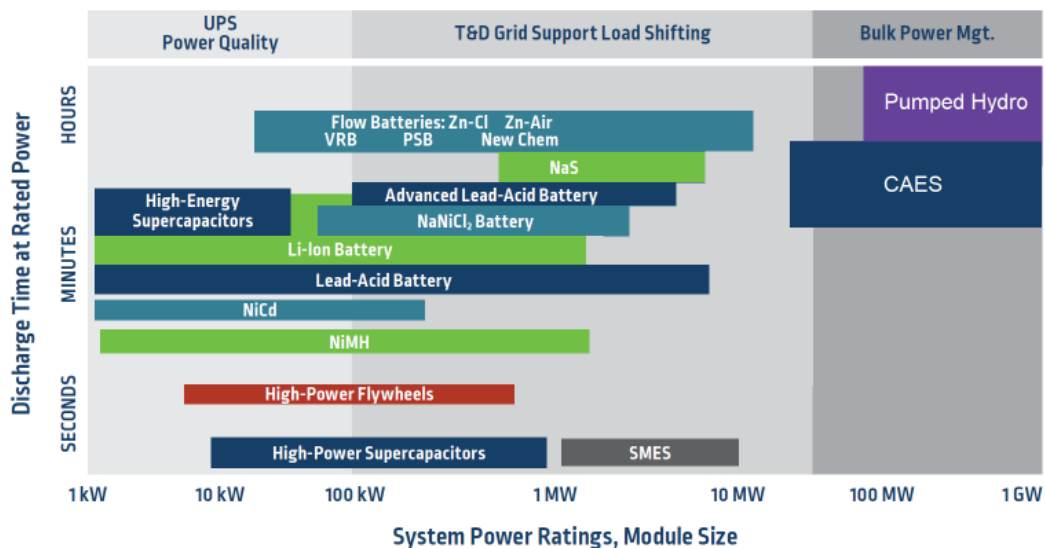


Figure 1.5. Positioning of Energy Storage Technologies [1.12].

Hydropower plays an important role in this context. For a long time, hydropower has been used because it is a renewable source with dominated technology. Studies and advances have been done to further improve this kind of generation. Figures 1.6 and 1.7 show the hydropower contribution to the energy mix throughout the world. Despite the fact that the graph presented in Fig. 1.6 is from 2016, the total installed capacity at the end of 2017 was 1,267 GW.

As long as hydropower plays an important role in the world energy mix, it is no wonder that the efficiency of its components have been an object of study in order to achieve its maximum potential. Severe rules have been considered in bids and acquisition contractual terms. For example, each 0.1% reduction in the efficiency of a new machine represents a 1% increase in the acquisition cost. It is also convenient to note the changing in regular loading cycles to meet renewables, which are of intermittent

nature, duty cycles. Treatment of such duty cycles is quite limited by today's machine standards.

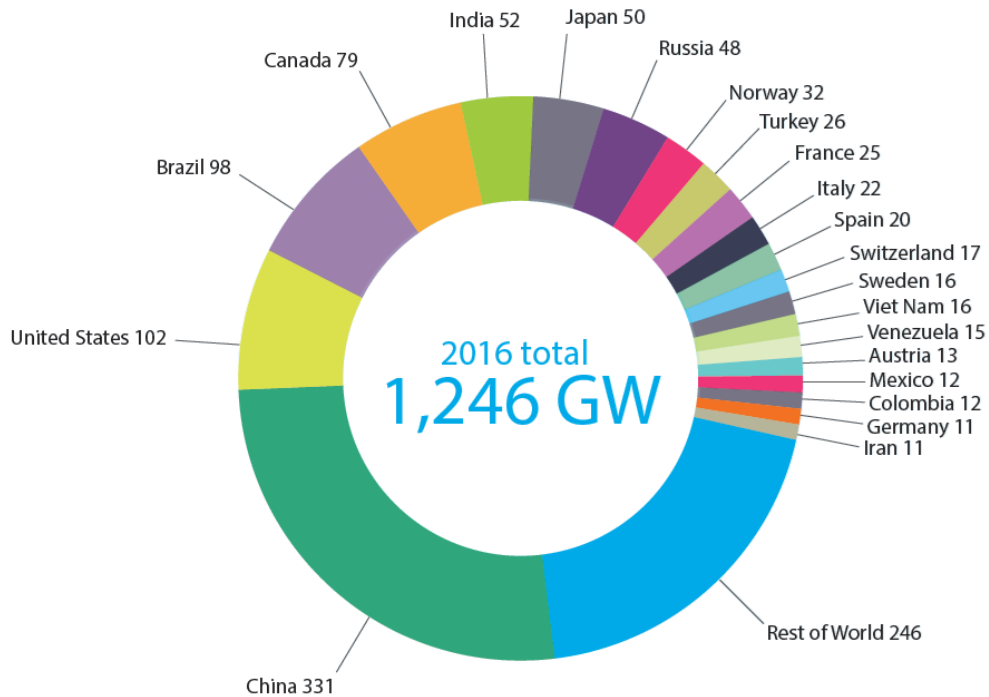


Figure 1.6. World installed hydropower capacity at the end of 2016 (including 150 GW pumped storage) [1.12].

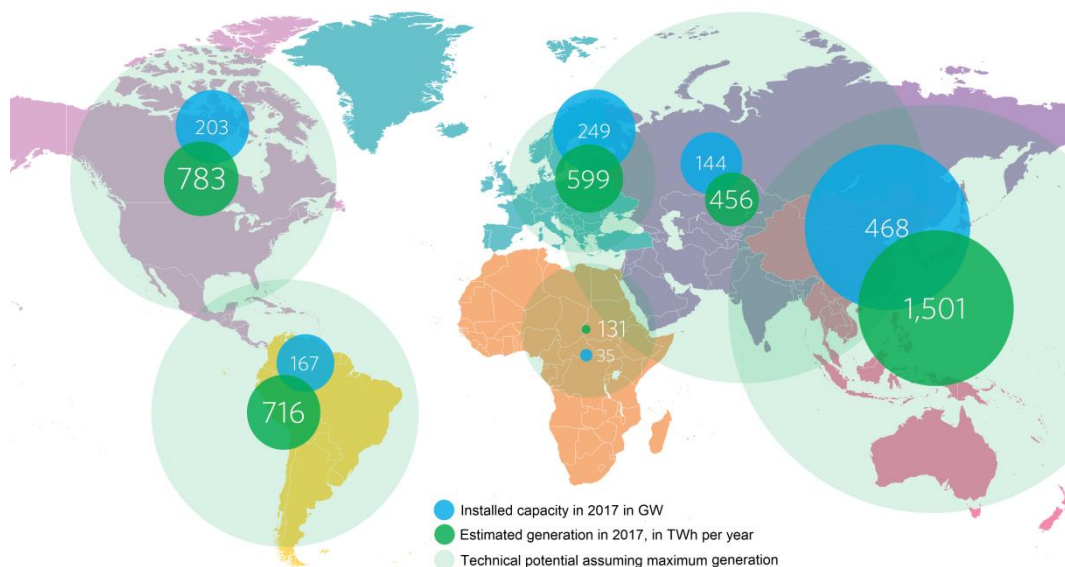


Figure 1.7. Hydropower capacity and generation by region at the end of 2017 [1.12].

The presented issues are intended to be enough to point out the need of more study on this subject. Thus, this study deals with each one of the presented questions and evaluates each of the weighted average efficiency in depth. In doing so, it obtains an

efficiency map over the capability chart of any such synchronous generator. After this introduction, the article can be divided into five chapters followed by the conclusions.

Chapter 2 brings forth the weighted average efficiency concept. As is shown, the present times require variable generation rather than the operation of the generator only at the nameplate rated condition. Issues such as resource availability, influence of variable, new renewable power generation, market rules and efficiency oriented design are discussed.

Chapter 3 is dedicated to efficiency and loss evaluation. The term efficiency is defined and an equation for its calculation as a function of input and output power is presented. Knowing that all of the energy transformation lies in losses, all of the different losses natures present in the synchronous generator energy conversion are considered and defined. In addition, the calculations of losses in any loading condition are presented as a function of the segregated losses obtained from tests at the rated loading condition.

An approach to the thermodynamic test, also known as calorimetric test, based on infrared thermal imaging is presented in Chapter 4. In this proposed method, it is considered that all of the losses are converted into heat and are released from the machine in transmission, convection, and radiation forms. This chapter shows the main equations and a special treatment in the heat transfer coefficient definition in addition to presenting a calculation. A proposed method of analysis of the acquired data is also covered in this chapter. The three running together necessary in order to find all of the segregated losses in the machine is also presented.

Chapter 5 is rendered to cover the capability chart basis and construction. The demonstrations come from simple vector diagrams and basic discussions and end in the drawing of the capability chart of a synchronous generator. The covered limits are the rotor heating, armature heating, practical stability, minimum excitation and core end heating. The latter have been less considered in salient pole synchronous generators rather than in the cylindrical rotor ones. Nevertheless, it has been considered and its being obtained in the light of the V curve family is presented.

Chapter 6 makes a combination of all of the aspects covered before with application to unit #6 of the Furnas hydropower plant generator. Tests were applied in order to determine the segregated losses at rated conditions. In addition to the no-load saturation curve, the field current for a given loading point is calculated, resulting in the family of V curves and the efficiency map of this generator. An analysis operation of this machine is presented, resulting in a 2D-Histogram representative of the operation of the machine. Eventually, the average efficiency weighted the percentage number of hours of operation in the several loading points is calculated for this machine. Chapter 6 is followed by conclusions and references.

## CHAPTER 2

### THE WEIGHTED AVERAGE EFFICIENCY CONCEPT

The rated efficiency of a synchronous generator is defined by its rated active power at the rated power factor. Nonetheless, it has been noticed that it is difficult to find a generator operating at rated conditions. The reason for such a statement may arise for several reasons. This chapter presents some arguments that sustain those reasons, discusses the efficiency oriented machine design, and introduces the concept of weighted average efficiency.

#### 2.1 The operation out from rated conditions

##### 2.1.1 The influence of new renewables

It is well known that wind and solar generation present great variability. Figure 2.1 and Fig. 2.2 respectively show wind and solar resource variation throughout a given year [2.1]. The correspondent generated power will eventually follow such variations. Many of the solutions point to energy storage systems. However, beyond batteries and other less common energy storage systems, hydropower plants have been seen as an effective way to store energy, or at least minimize the variations of the power available to the power system.

In this context, the generated power of a given hydropower plant will increase and decrease constantly over time in order to follow the new renewable variations. Therefore, when there is renewable power, the dispatched power of hydropower plant will remain low. If there is no available renewable power, the dispatched power of hydropower plant will be high. In short, the hydropower plant would work to complement the power generated to other renewable sources.

This variation of generated power imposes a duty cycle that is different from those duty types presented in IEC 60034-1 with sequential variation. The synchronous machine must be designed to afford this generated power variation followed by a constant temperature variation, bringing insulation problems and reducing the expected life time of the asset.

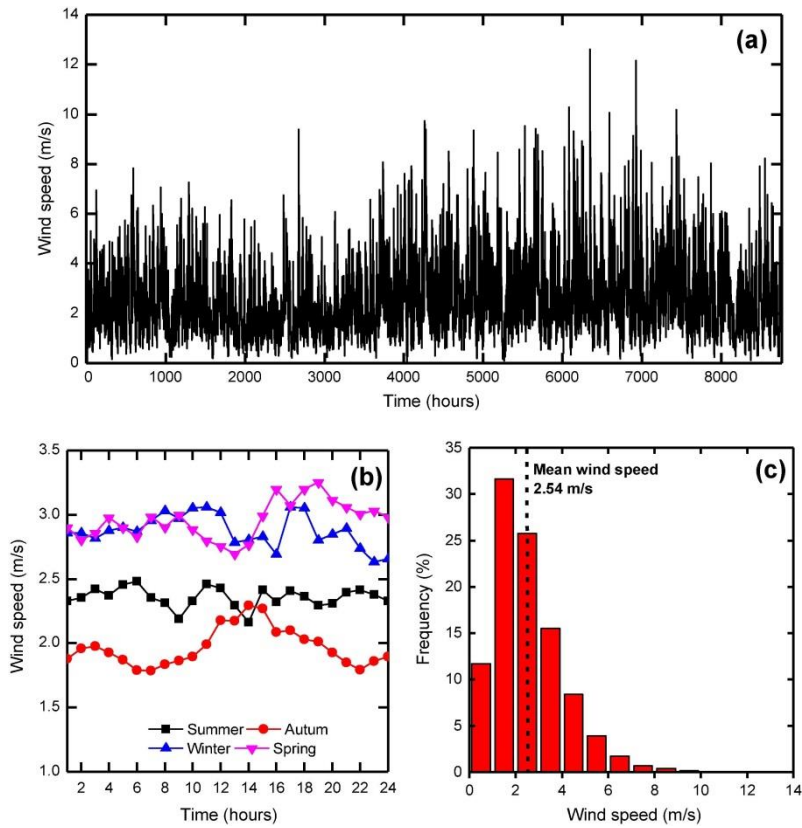


Figure 2.1. Wind variation over the course of one year [2.1]

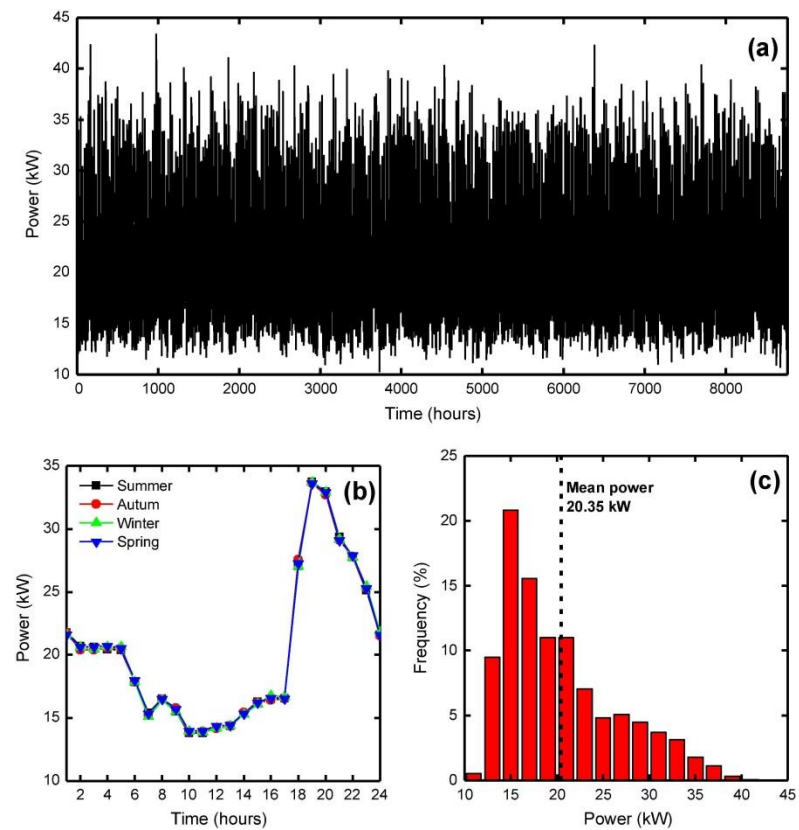
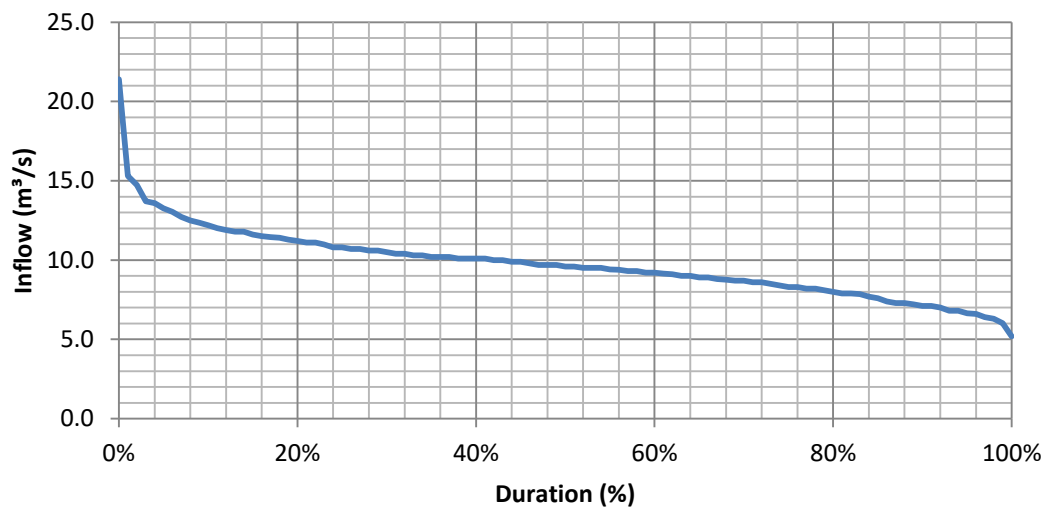


Figure 2.2. Solar power over the course of one year [2.1]

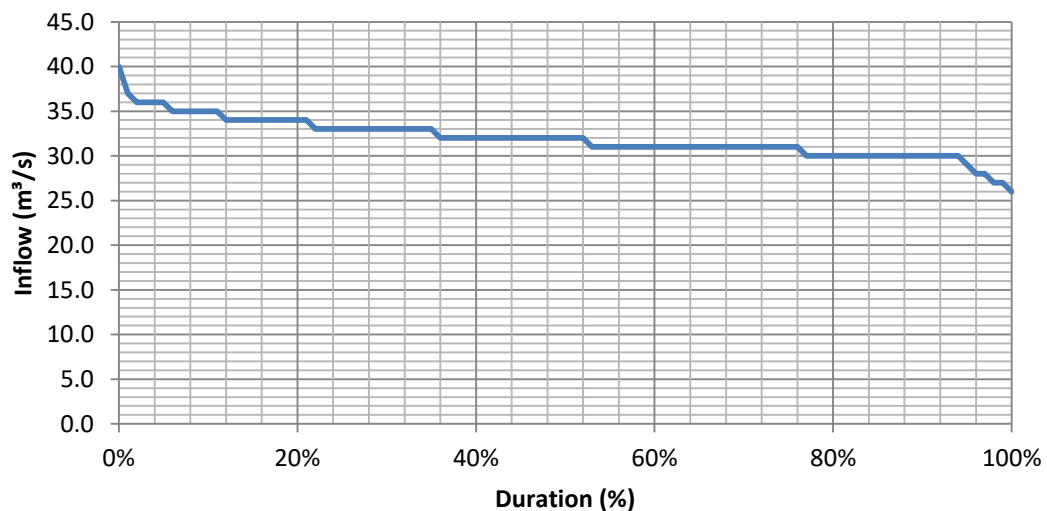
### 2.1.2 Energy issues

A hydro power plant depends on hydro resource availability, namely that of head and flow. It should be noted that, as a renewable power source, the hydropower plant is also subjected to resource availability. Of course the variations are much less than those in wind or solar generation. The degree of influence can be divided into two, depending on whether it is a run-of-river power plant or if it has a reservoir [2.2].

For run-of-river power plants, there is almost no variation in the available head but the active power generation is subjected to the availability of the inflows. The duration curve of inflows may be used to evaluate the flow variation as shown in Fig. 2.3.



(a)



(b)

Figure 2.3. Inflow variation of two different power plants.

The inflows for a power plant located in the headwaters of the basin, the Ouro River in the state of Bahia, Brazil, are shown in Fig. 2.3.a. The difference between maximum and minimum flow are noticeable. The curve shown in Fig. 2.3.b is almost flat and the difference between maximum and minimum flow is very low. The figure represents the inflows of the Formiga River in the state of Mato Grosso, Brazil. A reference index is the difference of the maximum to the minimum inflow over the average of the inflows. For the first case, the index is 1.668 while for the former case it is 0.439. This quite observably means that the power generated in the first case will have greater variations than that of the second case, which will remain nearly constant.

The variation of the inflows is also reflected in the variation of generated power and in the correspondent energy. Therefore, due to low inflows during some periods of a given year, the generator will work at a low power less than its rated power. Nevertheless, with high inflows, the generator will work at its full power.

This same question will be reflected in other issues such as the number of units in a power plant. If there is a lot of variation in the inflow, the hydro turbine must withstand the minimum flow in which case a great number of units may be necessary. When there is nearly no inflow variation, the number of units may be lower. The number of units can increase due to other technological-related reasons as is the case with the Itaipu hydro power plant. The hydropower plant is located at the end of the Paraná River with a natural regularization. As it is a plant of 14,400 MW, the total power must be divided among the 20 existent units in order to keep the power of each generator lower than the upper limit of design in the time of the hydropower plant construction.

Those questions, along with others that may be raised, are related to the run-of-river hydropower plants that do not have a reservoir. For those hydropower plants with reservoirs, the flow into the hydro turbine can be rather constant because the water is stored when there are high inflows and the water is released for the low inflows, keeping it quite constant. Therefore, the flow does not vary too much, but rather the head may vary with the inflows.

The graph shown in Fig. 2.3 demonstrates the variation of the gross head in a Furnas hydropower plant in Brazil while Fig. 2.4 presents the duration curve of the gross head. The significant variation of the net head over the years can be observed. The head variation can be explained in part by the reduction of inflows with the notorious climate change or due to the extreme usage of the stored water in the hydro cascade [2.3]. With the same proportion of flow, the head variation affects the generated power in a direct proportion. In the example presented, the gross head varies from approximately 80 m to about 100 m. Thus, a variation of at least 20% in the generated power is expected.

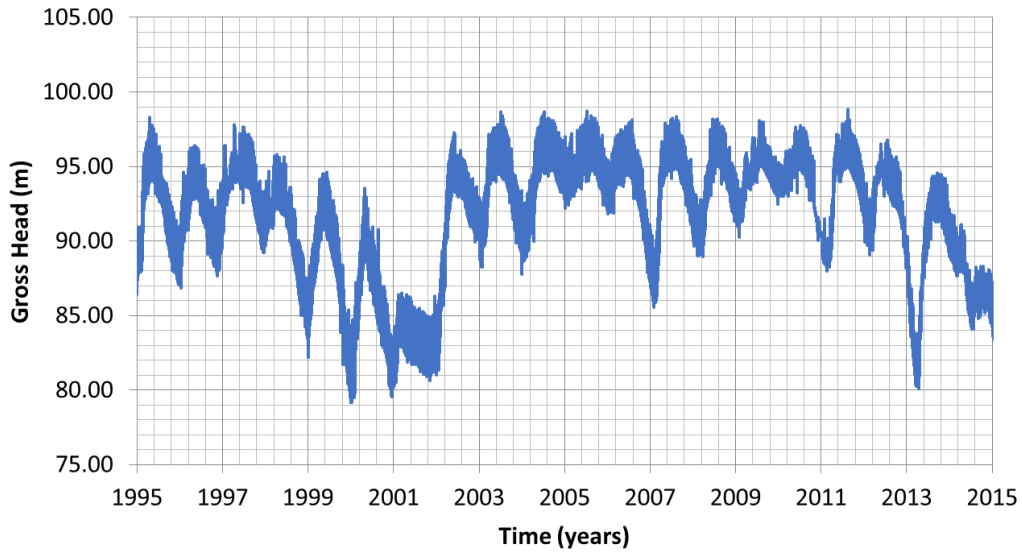


Figure 2.4. Gross head variation over time.

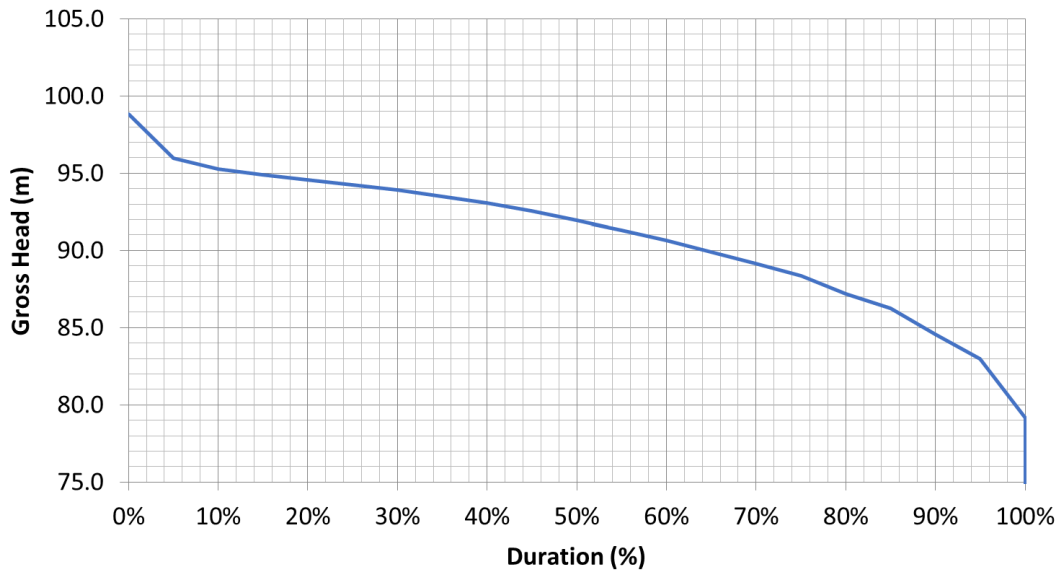


Figure 2.5. Gross head variation duration curve.

For a long time, the hydro turbines have been prepared for head and flow variations in the sense that their behavior in such situations is extremely well-known [2.4]. The so-called hill chart, presented in Fig. 2.6, depicts the efficiency of the turbine as a function of the discharge and head.

In the same way, the average efficiency of turbines, weighted by some different loads, is very commonly seen in the regular bids of generating equipment for hydropower plants.

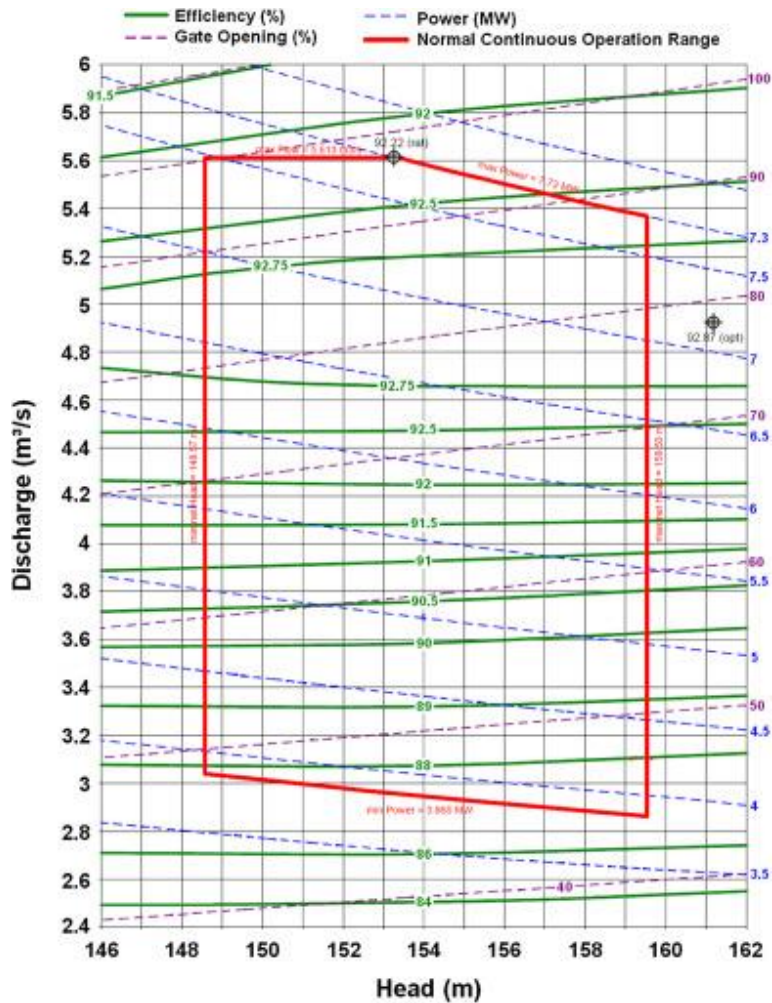


Figure 2.6. Operation chart of a hydro turbine.

### 2.1.3 Electricity market issues

While hydro power plant generation depends on the hydro resource availability, the final product, i.e., the generated energy, is sold on the electricity market at the current price. The term energy is applied to the active power over time while the reactive power may be paid as an auxiliary service in order to maintain the voltage in the power systems within acceptable values and attend stability issues.

The market premises are dependent on the country of study as each country develops its own rules to deal with this problem. There are many methods of monetary valuation. For instance, one method imposes fixed prices for the energy in which the power plant is reimbursed based on its firm energy and the monetization of any demanded reactive power is included in this price. As an alternative, the power plant's owner can deal straightforwardly with the consumer establishing the price for the energy. Another method is the so-called spot market where both producer and consumer negotiate energy prices in a chamber, generally to help solve either a surplus or a deficit problem. There are markets in which the price of energy is defined in an hourly basis, commonly known as TOU – Time-Of-Use.

Therefore, energy conversion efficiency, resource availability and the prices both for the energy and for the auxiliary services are in game. The loading of a generator must maximize the benefits along with the sale of energy. Of course, on the other side of this balance, and in center of the game, is the generator machine which must withstand the required generation variation, always bearing in mind its loss of life while staying under control.

## 2.2 Efficiency oriented design

Many design factors have an influence on the machine rated efficiency, which is dependent on the various types of losses that occur inside the machine during the energy conversion. The efficiency-oriented design is a design of the machine taking into account the most probable points of operation. It means that the highest efficiency will be sought to meet the most probable operating points.

The distribution of the losses is very important because it will dictate to efficiency not only in the rated point, but also in its behavior in all of the operation areas. Of course it depends on the design of the machine since each design will eventually result in a loss distribution.

It is common to consider the Esson Factor ( $c$ ) in the dimensional analysis of a generator while designing a rotating machine [2.5]. The equation involving the Esson Factor is shown in (2.1) and establishes that the power ( $S$ ) of a machine is proportional to its pseudo-volume given by the active length ( $L$ ) times the square of the bore diameter ( $D$ ) and to the speed ( $n$ ). Two alternatives are shown in Fig. 2.7.

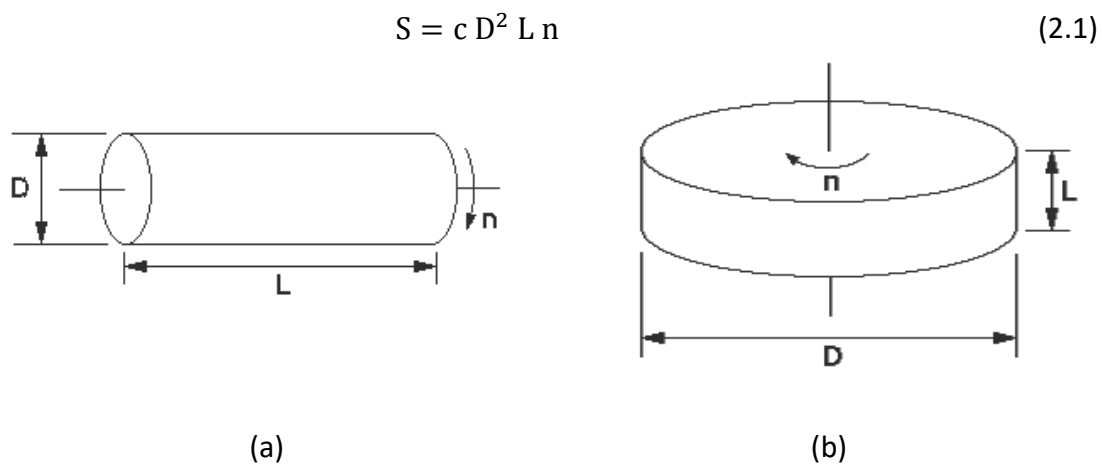


Figure 2.7. Dimensional analysis of a generator.

While the horizontal shaft arrangement depicted in Fig. 2.7.a is common to turbo-generators and hydro-generators with speeds greater than roughly 300 rpm, the vertical shaft approach presented in Fig. 2.7.b is applicable to hydro-generators of lower speeds.

Even for same power, speed, and Esson Factor, the manufacturer has great flexibility in the design, being able to choose the most convenient active length, bore diameter, and core material. Nonetheless, many other variables are also subject to evaluation and adjustments, such as the airgap length, stator and rotor windings current density and resistances, insulation, stator and rotor yokes lengths, and saturation.

It is convenient to notice that when a greater diameter is chosen, the periphery speed will increase and, as a consequence, the windage loss (viscous friction) and that the necessary power absorbed to move the airflow will also increase.

$$v = \frac{\pi}{60} D n \quad (2.2)$$

Where  $v$  is the periphery speed (m/s),  $D$  is the core diameter (m) and  $n$  is the rated speed (RPM).

Empirical equation for windage loss ( $P_W$ ) calculation is [2.6]:

$$P_W = Q_{\text{air}} (\Delta P_{\text{air}} + \Delta P_{\text{hex}}) \frac{1.21}{\eta_V} 10^{-3} + P_{\text{vf}} \quad (2.3)$$

Where  $P_W$  is the windage loss (W),  $Q_{\text{air}}$  is the air flow ( $\text{m}^3/\text{s}$ ),  $\eta_V$  and is the ventilator efficiency.  $\Delta P_{\text{air}}$  and  $\Delta P_{\text{hex}}$  are the pressure drop in the air and in the heat exchanger ( $\text{N}/\text{m}^2$ ):

$$\Delta P_{\text{air}} = \frac{\rho}{2} v^2 \left\{ 1.85 L + \left[ 2.35 + \frac{2}{5} \left( \frac{v_{\text{air}}}{v} \right)^{1.75} \right] \right\} \quad (2.4)$$

Where  $\rho$  is the air density ( $\text{kg}/\text{m}^3$ ) at the temperature of operation,  $L$  is the core active length (m), and  $v_{\text{air}}$  is the air velocity (m/s).

The losses with viscous friction may be given by:

$$P_{\text{vf}} = 5.6 D_G^4 n^3 (0.1 D + L) \quad (2.5)$$

Where  $D_G$  is the diameter over the airgap line (m).

While the bearings loss remains almost constant as long it does not depend on the machine dimensions and is external to the machine, the windage loss will vary with the diameter raised to the fourth power. Such a happening is of bold importance. It is expected that the percentage of the windage loss may increase to the fourth power of the percentage rotor diameter increase. With the diameter increase maintaining power and voltage as constants, it is expected that the field current, both at no-load and at rated conditions, will also increase.

It is explained, at least in part, that as long as the output power, speed, and Esson Factor remain constant, then so too will the pseudo-volume ( $D^2L$ ) also be constant (2.1). The active length reduction is proportional to the inverse of the squared diameter increase. Likewise, the active area ( $A$ ) is inversely proportional to the diameter increase.

$$L_2 = L_1 (D_1/D_2)^2 \quad (2.6)$$

$$A_2 = A_1 D_1/D_2 \quad (2.7)$$

Thus, in order to maintain the output voltage, the excitation current percentage must increase in approximately the same proportion as the percentage rotor diameter increases. Despite the rotational speed remaining constant, it is also expected that the percentage increase in the mechanical friction loss due to the field current increase.

An increase in the excitation current does not directly imply in the rotor current loss as it is also dependent on the rotor resistance. Ultimately, the field current loss variation is proportional to the resistance variation and the square of the field current variation.

The same reasoning should be applied to the stator current losses. Considering the basic premise adopted here, with the power and voltage being the same, the stator current loss will depend on whether the resistance in the stator will remain the same or not.

In maintaining the core material, the losses in the core will vary within the flux and dimensions of the stator yoke and teeth. If the dimensions remain the same, the loss in the core material tends to increase to a larger diameter.

In order to illustrate the aforementioned establishments, two different designs were compared. The compared machines have the same rated characteristics but different dimensions, i.e., the second machine has an active length of about 25% smaller than the first machine, resulting in a greater diameter, different construction, magnetic, and loss characteristics. Table 2.1 depicts the rated characteristic of the machines while Table 2.2 shows the changes in fundamental quantities.

Table 2.1. Rated quantities of studied machines

Symbol	Quantity	Unit	Value
S	Apparent power	MVA	100
V	Voltage	kV	13.8
PF	Power factor	-	0.85
I	Current	A	4184
n	Rotational speed	RPM	257.14

Table 2.2. Fundamental quantities behavior

Symbol	Quantity	Unit	#1	#2	Variation
L	Stator active length	mm	2500	1870	-25.20%
D	Stator bore diameter	mm	5200	6000	15.38%
$I_{F0}$	No-load field current	A	374	427	14.17%
$I_F$	Full load field current	A	753	862	14.48%
$R_A$	Stator resistance	$\Omega$	0.0033032	0.003284	-0.58%
$R_F$	Rotor resistance	$\Omega$	0.2369	0.177	-25.28%
$\Delta\theta$	Air cooling temperature increase	K	30.8	27.5	-10.71%
v	Periphery speed	m/s	70.01	80.78	15.38%

The diverse losses will change as the dimensions change. This will affect not only the rated efficiency, but also the efficiency along all of the operating area delimited by the capability chart. The diverse kind of loss and its behavior is depicted in Table 2.3 whereas the total loss and efficiency in rated condition are presented in Table 2.4.

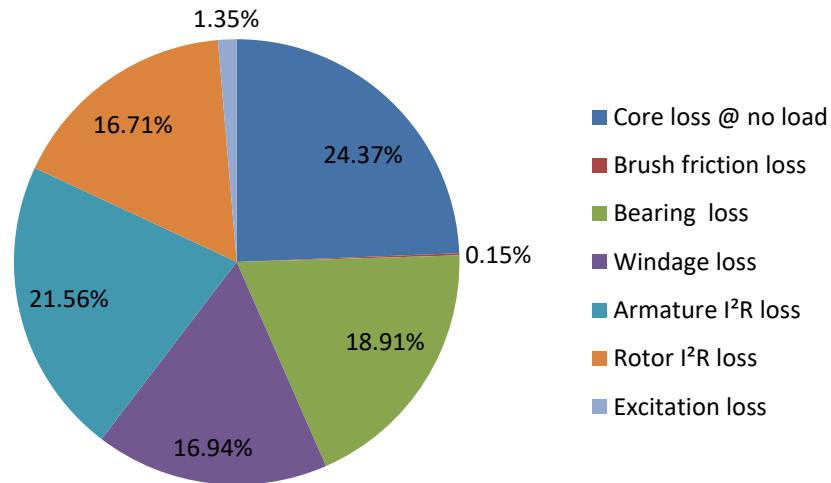
Table 2.3. Losses behavior

Symbol	Quantity	Unit	#1	#2	Variation
$P_C$	Core losses	kW	238.4	258.8	8.56%
$P_{br}$	Brush mechanical friction loss	kW	1.5	1.7	13.33%
$P_B$	Bearing loss	kW	185	185	0.00%
$P_W$	Windage loss (total)	kW	165.7	287.4	73.45%
$P_{SC}$	Armature current loss (@ 75 °C)	kW	210.9	209.7	-0.57%
$P_{RC}$	Rotor current loss (@ 75 °C)	kW	163.5	159.7	-2.32%
$P_E$	Excitation loss	kW	13.2	12.9	-2.27%
$P_S$	Stray-load loss	kW	136	138.9	2.13%

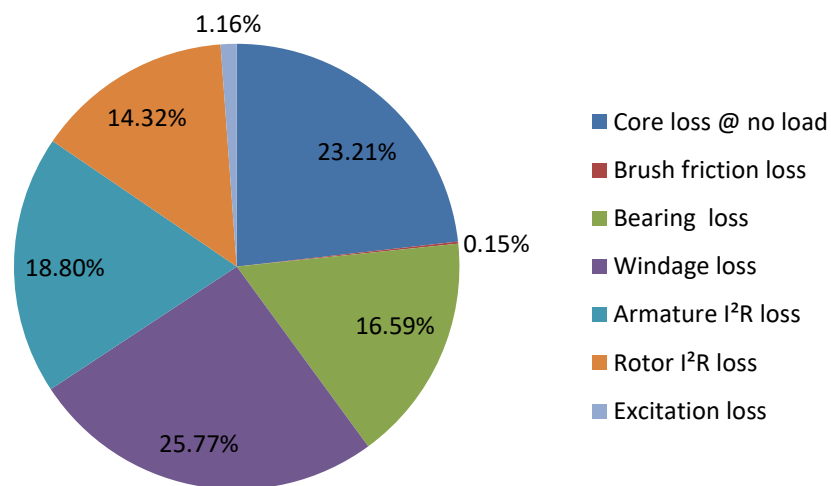
Table 2.4. Total losses and efficiency behavior

Symbol	Quantity	Unit	#1	#2	Variation
$P_T$	Total loss	kW	1114.2	1254.1	12.56%
H	Efficiency	%	98.71%	98.55%	-0.16%

In the two previously discussed projects, the stator and rotor windings current density and resistances, insulation, along with their stator and rotor yokes, remained constant. The bearings loss was the same in both cases. Figure 2.8.a and 2.8.b respectively show participation graphs of each loss in the total loss in both cases.



(a)



(b)

Figure 2.8. Losses participation in the total loss.

The diameter increased by about 15% from the first design to the second design. This means that the periphery speed has a percentage increase of the same amount. When this percentage is raised to the fourth power, it results in 74.9%, which is almost the same amount of the increase in the windage loss. The core loss increased as there were no modifications in the armature and rotor yokes, as can be seen in Fig. 2.9.

As long as there was no variation in the armature current, the stator loss followed the variation in the stator resistance of about -0.58%. As previously explained, the field current increased in the same proportion of the stator diameter increase. Therefore, the brush mechanical friction loss increased in the same proportion.

Despite a field current increase of about 14.5%, the current loss in the field circuit reduced by about 2.3%. This can be at least partially explained by the field rotor resistance reduction of 25%. In fact, the squared increase in the field current multiplied by the 25% reduction in the field resistance will result in an overall reduction of -2.1% in the field current loss.

Figure 2.9 presents the percentage magnitude losses variation between the two designs. The Fig. 2.10.a and 2.10.b shows the comparison of the machines #1 and #2, with same nameplate characteristics but with different diameters, 5200 mm and 6000 mm.

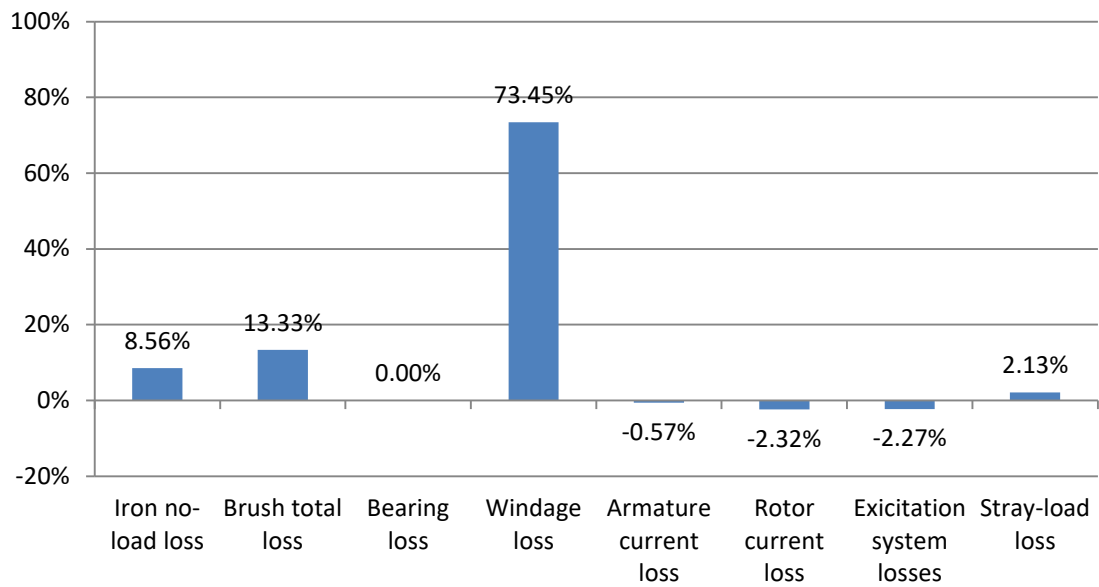


Figure 2.9. Percentage magnitude losses variation

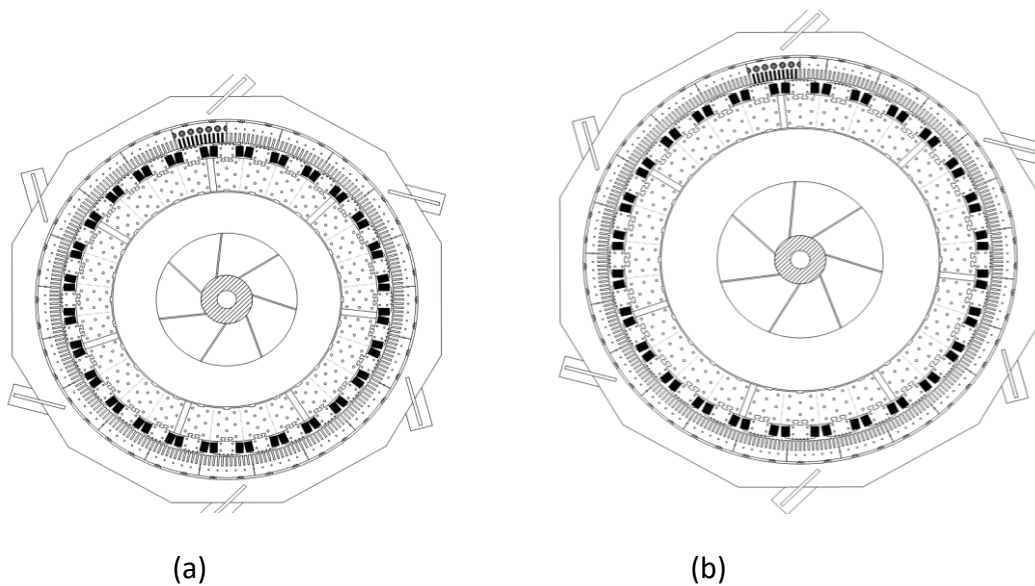


Figure 2.10. Machines cross-sections with proportional dimensions.

### 2.3 Weighted average efficiency

It was recognized that a modern machine should afford a high number of stop-start cycles; it ought to operate over the load range, but infrequently at a rated load; and allow a high share of reactive power for grid stabilization with full use of the under-excitation capability.

Extending considerations beyond the impact of the duty cycle, the impact of variable loading on other specified generator characteristics, such as efficiency, was also considered. This may be of particular interest and concern in cases where the generator is being specified for replacement of an existing unit, independent of the prime mover, for example. In such cases, comparison of generator efficiencies explicitly may weigh on the equipment selection whereas for most cases in which both the prime-mover and generator are supplied as a package, the combined efficiency is of primary consideration.

With large variations in load, generator losses vary, resulting in significant changes in generator efficiency. While the overall generating plant efficiency is largely dictated by the cycle thermal efficiency, a review of the generator's losses versus load is instructive.

In this context, the weighted average efficiency plays a very important role. In the past, the efficiency measurement at a given point, in general the rated power, was enough. Nowadays, due to the several established arguments in this document, it was realized that a generator operates at several points, and therefore, the knowledge of the energy conversion efficiency at those points is important, just like the knowledge of efficiency at the rated condition.

Considering rated voltage, speed, and frequency under balanced load conditions, the weighted average efficiency shall be calculated according to the following formula.

$$\eta_w = \sum_{k=1}^n A_k \eta_k \quad (2.8)$$

Where

$$\sum_{k=1}^n A_k = 1 \quad (2.9)$$

Where  $\eta_w$  is the weighted average efficiency,  $n$  is the number of loading points at rated voltage, rated speed and specified power factors.  $A_k$  is the weighting factor at specified power factors, and  $\eta_k$  is the efficiency corresponding to each loading point.

New versions of recognized standards, such as IEC 60034-33 [2.7] and IEEE C50.12 [2.8], will consider the weighted average efficiency.

In the approach adopted in this study, the weighted average efficiency is obtained from two referent pieces of information: the efficiency map and the 2D-Histogram of the loading.

The efficiency map is obtained from the loss segregation at the rated point and the no-load saturation curve. These are tests that are often utilized when acquiring a generator. From the no-load saturation curve, the excitation current for any active and reactive pair loading can be obtained. Therefore, the losses dependent on the excitation current can be calculated. Of course, the armature current is dependent on the active and reactive loading powers, and the losses dependent on the armature current that can be readily calculated. Thus, the efficiency for any active and reactive loading powers can be calculated, resulting in the so-called efficiency map.

The 2D-Histogram is evaluated by the probability of finding a synchronous generator working in a given active and reactive loading powers. It is a constructed history of generator operation, in general, for each hour of an entire year, resulting in 8,760 active and reactive power pairs. This may be possible for existent generators that are already installed in the field. For new generators, recently purchased or while in the bidding process, few points may be specified with their respective weight over their efficiency.

The information obtained through the efficiency map is crossed with the information raised in the 2D-Histogram. Each active and reactive loading point has its efficiency and probability. The multiplication of these two values will result in the efficiency weighted by the time length of this single point. The summation of the efficiency weighted by the time length for the several points within the capability chart will eventually result in the weighted average efficiency.

Consider the example presented in Fig 2.11. The figure presents a capability chart of a 1000 MVA+ rounded pole synchronous generator [2.9-2.12]. Within the capability chart, there are several lines of the same efficiencies. The yellow boxes represent the most important points of operation of this machine. Inside each box there is the weight of each point. It is worth mentioning that this machine was not yet constructed or even installed; therefore, the contents of each yellow box represent the expected percentage number of hours of operation of this machine at this point. The sum of the number in the yellow boxes must be 100%. The rated efficiency is 99.96% while the weighted average efficiency is 99.08%, i.e., 0.12% more than that exhibited at the rated load.

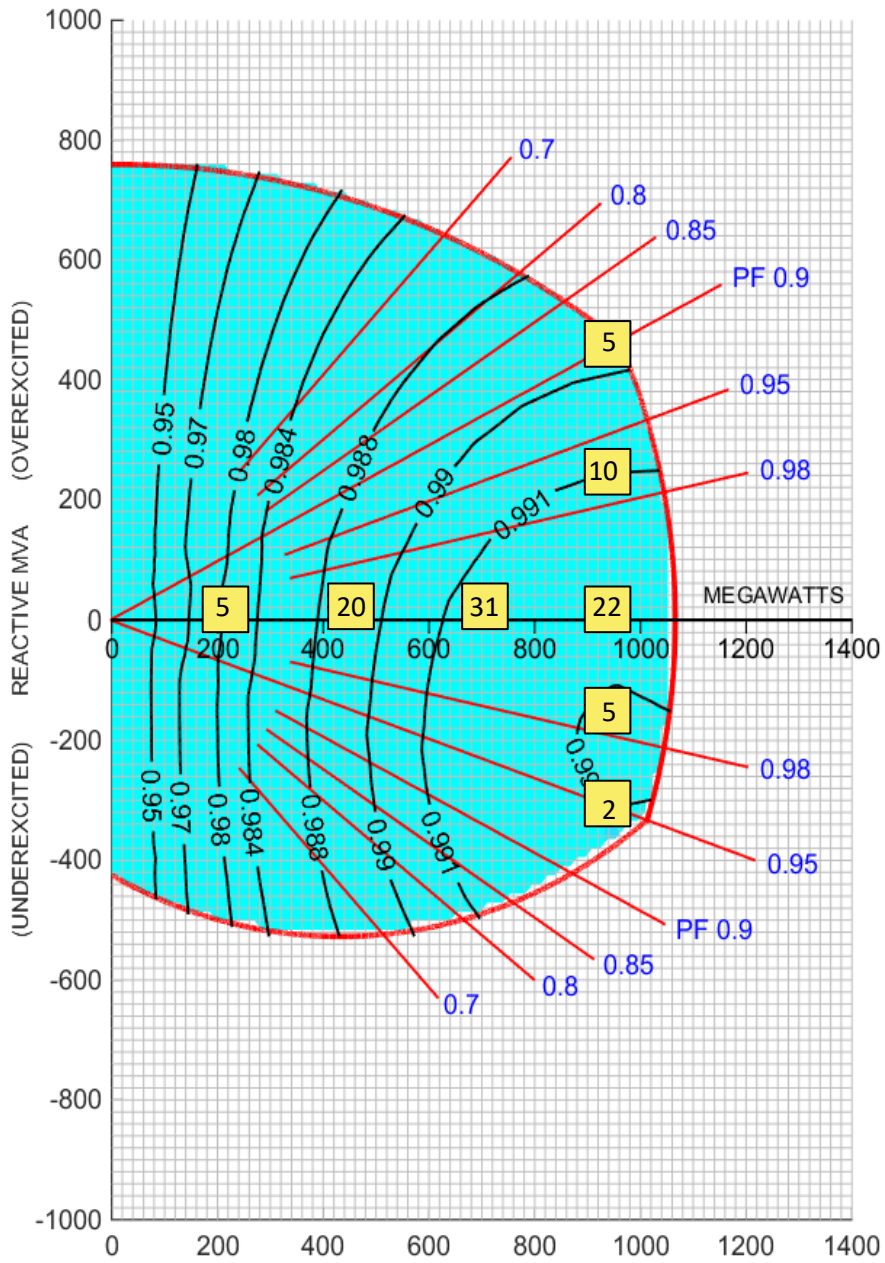


Figure 2.11. Efficiency contour, considering loading and weights.

## CHAPTER 3

### MACHINE LOSSES AND EFFICIENCY

#### 3.1 Efficiency and losses definitions

The efficiency ( $\eta$ ) of any energy conversion system is the relation between the output ( $P_o$ ) and the input ( $P_i$ ) of this system as described in (3.1).

$$\eta = \frac{P_o}{P_i} \quad (3.1)$$

Equation (3.1) is the base for calculating the efficiency using direct methods and is always applied to active power.

It is worth mentioning that the use of the direct method, when the efficiency is high, involves the measurement of input and output powers of approximately the same order. The unavoidable measurement errors tends to fall upon both input and output power measurements, leading to considerable inaccurate results.

On the other hand, the difference between input and output powers is a result of power losses ( $P_l$ ) inherent to any energy conversion system. For a generator, the input power is of mechanical nature while the output power is of electrical nature. The mechanical power is a product between torque and speed. While speed is often reasonably easy to measure, torque is very difficult, which often leads to large errors. Therefore, writing the input power as a function of the output power and losses, one can obtain the result.

$$\eta = \frac{P_i - P_l}{P_i} = \frac{P_o}{P_o + P_l} \quad (3.2)$$

The determination of the power losses is the heart of the indirect efficiency test methods.

#### 3.2 The diverse nature of the losses

The losses in a synchronous generator have several natures. The total loss is the summation of the individual loss which is characterized as follows [3.1-3.3].

##### 3.2.1. Current losses in the armature ( $P_{SC}$ )

This kind of loss is due to the AC current flowing in the resistive armature windings. It is dependent on the armature resistance and on the square of the effective armature current.

### 3.2.2. Current losses in the rotor ( $P_{RC}$ )

Such losses are due to the DC current flowing in the resistive rotor winding. This is dependent on the field resistance and on the square of the field current.

### 3.2.3. Stator core losses ( $P_C$ )

In general, the core losses correspond to the hysteresis and eddy currents. The hysteresis comes from the current cycle and the residual flux in the magnetic material whereas the eddy currents correspond to induced currents in the magnetic core and are of an  $I^2R$  nature.

### 3.2.4. Stray-load losses ( $P_S$ )

This loss is of magnetic nature in the stator core and of eddy current losses in the primary winding conductors. It increases with the loading of the machine since fluxes tend to close with different metal parts rather than the core of the machine, such as enclosure, shaft, and others. It is often called a supplementary or additional loss.

### 3.2.5. Windage losses ( $P_W$ )

This loss is due to the self-ventilation and drag forces in the rotating parts of the machine. For generator efficiency calculation purposes, the drag forces of any existent flywheel must be disregarded.

### 3.2.6. Excitation losses ( $P_E$ )

In an ideal world with no losses, the output power of a generator is the generated power subtracted by the excitation power ( $P_E$ ). Nevertheless, the excitation power is summed-up with the prime mover power, resulting in the output power being equal to the prime mover power, as depicted in Fig. 3.1.

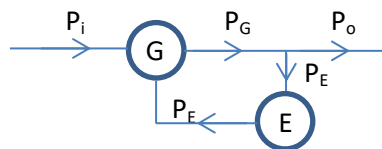


Figure 3.1. Power flow considering excitation power.

$$P_o = P_G - P_E \quad (3.3)$$

and

$$P_G = P_i + P_E \quad (3.4)$$

Therefore,

$$P_o = P_i + P_E - P_E = P_i \quad (3.5)$$

However, in the real world, with losses in energy conversion in the generator ( $\eta_G$ ) and in the excitation system ( $\eta_E$ ), there will be:

$$P_o = P_G - P_E \quad (3.6)$$

and

$$P_G = \eta_G P_i + \eta_E P_E \quad (3.7)$$

Therefore,

$$P_o = \eta_G P_i + \eta_E P_E - P_E = \eta_G P_i - (1 - \eta_E) P_E \quad (3.8)$$

The term  $(1 - \eta_E)$  represents the loss in the excitation system. In other words, it represents excitation loss, which comprises all the loss in any excitation system.

It can be observed that these equations are valid only if the output power is measured after the excitation power tap. If the output power is measured before the excitation tap, the power of the excitation must be added as an input power to the generator, and the equation of the generator efficiency will be (3.9).

$$\eta_G = \frac{P_o}{P_i + P_E} \quad (3.9)$$

### 3.2.7. Brush losses ( $P_{br}$ )

This loss is due to the excitation current circulation over the brushes resulting in a voltage drop in the brushes, and is given by:

$$P_{br1} = k V_F I_F \quad (3.10)$$

Where  $P_{br1}$  is the loss due to voltage drop in the brush (W),  $V_F$  is the excitation voltage (V),  $I_F$  is the excitation current (A),  $k$  is proportionality quantity valuing either 2 for a graphite based brush or 0.6 for a metal based brush.

There is also friction loss due to the contact of the excitation brushes with the collecting rings, which are calculated as follows.

$$P_{br2} = 0.6 A v \quad (3.11)$$

Where  $P_{br2}$  is the brush loss due to friction (W),  $A$  is the total slipping area in a single ring ( $\text{cm}^2$ ), and  $v$  is the periphery speed (m/s).

### 3.2.8. Bearing losses ( $P_B$ )

There are bearings in the generation set that belong to the prime mover and bearings that belong to the generator. These losses are related to the bearings that belong only to the electrical machine. This loss is due to the friction between the shaft and the generator bearings.

### 3.3 Determination of the losses for any loading condition

The approach adopted in this study accesses the losses based on the losses measured in a given loading reference condition. The constant and variable losses are calculated as follows.

#### 3.3.1 Constant losses

The constant losses are those in which there is no variation in the machine loading. They are composed by the windage loss, armature core loss, and friction loss.

The windage loss is proportional to its speed cubed. Thus, it is considered a constant since the machine acting as a generator in a hydro power works at a constant speed to achieve the constant frequency of the system.

The armature core loss is proportional to the frequency and applied voltage. As both frequency and voltage are almost constant, the core loss is also considered constant.

There is little variation of friction loss with the loading of the machine. However, as long as the major effort is due to the turbine axial force, and it is considered almost constant, the friction loss will also be considered constant.

#### 3.3.2 Armature current dependent losses

The armature current dependent losses are the armature copper loss and the stray load loss. Both of them vary with the square of the armature current. The armature current is calculated from the any loading condition:

$$I_A = \frac{\sqrt{P^2 + Q^2}}{\sqrt{3} U_A} \quad (3.12)$$

Where  $P$  and  $Q$  are the active (W) and reactive (var) loading powers, and  $U_A$  is the armature terminal line voltage (V).

Note that a correction for the temperature must be applied to the armature copper loss due to the resistance variation.

### 3.3.3 Field current dependent losses

Field current dependent losses are the copper loss, voltage drop in the brushes, and excitation loss. The first two losses vary with the square of the field current whereas the third loss is proportional to the field current.

The field current is calculated using de Potier reactance. Given  $X_{du}$ ,  $X_{qu}$ ,  $X_P$ , and  $R_A$ , the following sequence is used [3.1].

a) Calculating the loading angle:

$$\delta = \tan^{-1} \left( \frac{I_A R_A \sin \varphi - I_A X_{qu} \cos \varphi}{U_A + I_A R_A \cos \varphi + I_A X_{qu} \sin \varphi} \right) \quad (3.13)$$

Where  $\varphi$  is the power factor angle, given by:

$$\varphi = \tan^{-1}(Q/P) \quad (3.14)$$

c) Calculating the induced voltage:

$$E_{GU} = U_A \cos \delta + R_A I_A \cos(\delta + \varphi) + X_{du} I_A \sin(\delta + \varphi) \quad (3.15)$$

Using the no-load saturation curve, on the airgap line, the value of  $I_{FU}$  can be obtained based on the calculated  $E_{GU}$ . Considering the approach presented in [3.4],  $I_{FU}$  is:

$$I_{FU} = E_{GU}/b_V \quad (3.16)$$

d) The angle of the Potier voltage is:

$$\theta = \tan^{-1} \left( \frac{I_A R_A \sin \varphi - I_A X_P \cos \varphi}{U_A + I_A R_A \cos \varphi + I_A X_P \sin \varphi} \right) \quad (3.17)$$

e) The effective voltage back of Potier reactance

$$E_P = U_A \cos \theta + R_A I_A \cos(\theta + \varphi) + X_P I_A \sin(\theta + \varphi) \quad (3.18)$$

e) Calculation of  $I_{FS}$

The field current  $I_{FS}$  is the difference from the saturation curve to the airgap line. Considering the saturated part of the saturation curve modeled as a second order polynomial, it is [3.4]:

$$I_{FS} = \left( \sum_{i=1}^n b_i E_P^i \right) - \frac{E_P}{b_V} \quad (3.19)$$



### 3.4. Losses and efficiency calculation for any load

Once segregating losses for the rated condition is done, the losses in other conditions can be calculated. The variation of the losses generally depends on the current squared, such as copper losses, in the armature and in the rotor, as was previously mentioned. Nevertheless, other losses also vary with the square of the current, such as the stray load loss and the loss in the brushes, as recognized by the Standard IEEE 115, which brings the following graph shown in Fig. 3.3.

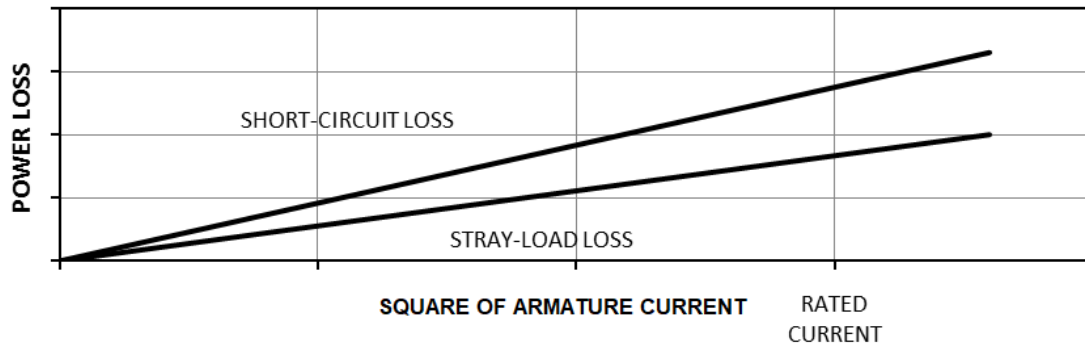


Figure 3.3. Stray-load loss variation according Standard IEEE 115 [3.1].

The excitation power, on the other hand, is proportional to the field current, and the core loss is proportional to the armature voltage, in the region from zero to the rated armature voltage, as depicted in Fig. 3.4 from IEEE Standard 115.

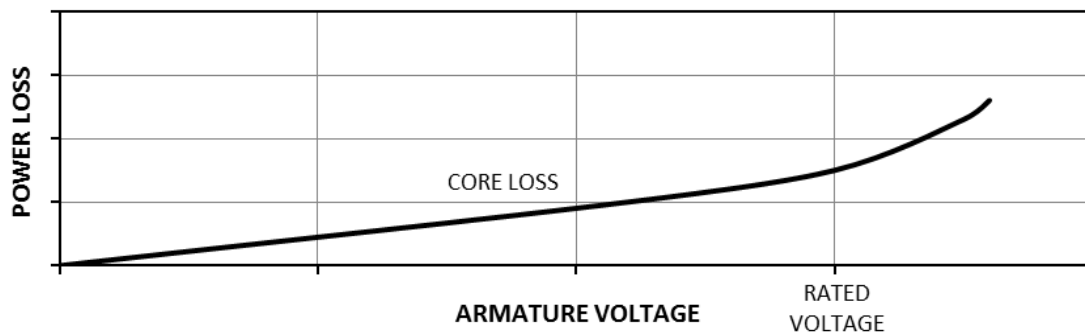


Figure 3.4. Core loss variation according to Standard IEEE 115 [3.1].

The relations are depicted as follows.

$$P_{SC} = P_{SC}^* \left( \frac{I_A}{I_A^*} \right)^2 \quad (3.21)$$

$$P_{RC} = P_{RC}^* \left( \frac{I_F}{I_F^*} \right)^2 \quad (3.22)$$

$$P_S = P_S^* \left( \frac{I_A}{I_A^*} \right)^2 \quad (3.23)$$

$$P_C = P_C^* \left( \frac{U_A}{U_A^*} \right)^2 \quad (3.24)$$

$$P_{br} = P_{br}^* \left( \frac{I_F}{I_F^*} \right)^2 \quad (3.25)$$

$$P_E = P_E^* \left( \frac{I_F}{I_F^*} \right) \quad (3.26)$$

### 3.5. Efficiency calculation

Some of the losses are constant and others are variants that are calculated. Therefore, the final efficiency may be calculated as:

$$\eta = \frac{P_o}{P_o + P_{SC} + P_{RC} + P_C + P_S + P_W + P_E + P_{br} + P_B} \quad (3.27)$$

## CHAPTER 4

### INFRARED-BASED CALORIMETRIC METHOD

The practical determination of the energy conversion efficiency of a synchronous generator is of utmost importance for both manufacturers and end users that are interested in calibrating their design techniques and surviving acceptance tests, respectively. In addition, efficiency indicates how a primary source has been utilized and thus it can work as a good threshold for maintenance procedures.

As stated before, the efficiency of any energy conversion system is the relation between the output and the input of this system which forms the basis of the direct efficiency test methods along with the difference between input and output powers, which result in the power losses that are inherent to any energy conversion system. The determination of the power losses is the heart of the indirect efficiency test methods.

As long as the input power can be obtained by the summation of the output power with the power loss, efficiency ( $\eta$ ) can be calculated as follows. For synchronous machines of hydro power plants, the measurement of the output electric power ( $P_o$ ) is simpler than the input power ( $P_i$ ), which is mechanical in nature, resulting in (4.1).

$$\eta = \frac{P_o}{P_i} \quad (4.1)$$

For a generator, the input power is of mechanical nature while the output power is of electrical nature. The mechanical power is a product between torque and speed. While speed is often reasonably easy to measure, torque is very difficult and often leads to large errors.

Indirect methods, on the other hand, bring the advantage of measuring only one high power (output) and one relatively small power (losses). As long as the errors involved in loss determination are proportionally reduced, a lower overall uncertainty regarding the efficiency measurement will eventually be obtained. Equation (4.2) presents the efficiency as a function of the output power and losses ( $P_l$ ).

$$\eta = 1 - \frac{P_l}{P_o + P_l} \quad (4.2)$$

Losses segregation methods such as retardation and calorimetric techniques are described by the most popular standards [4.1-4.2]. Losses determination has been the subject of several such recent efforts.

Some of the recent studies have applied the calorimetric method of loss determination on small motors in a laboratory [4.3-4.4]. Theoretical models for studying some losses of the synchronous machines have been developed, showing a good agreement with test results [4.5-4.6]. Application of the calorimetric method in a hydropower plant is presented in [4.7-4.8]. Unfortunately, none of the previous studies have been focused on the evolution of the calorimetric method, its theory, nor its application.

The contribution of this study relies on the application of the calorimetric method in order to determine the efficiency of energy conversion of synchronous machines in situ. Infrared thermal imaging is used to determine released losses through the machine surface as shown in Fig. 4.1. A different approach to define the heat transfer coefficient and the consideration of conduction losses in the generator shaft are also presented.

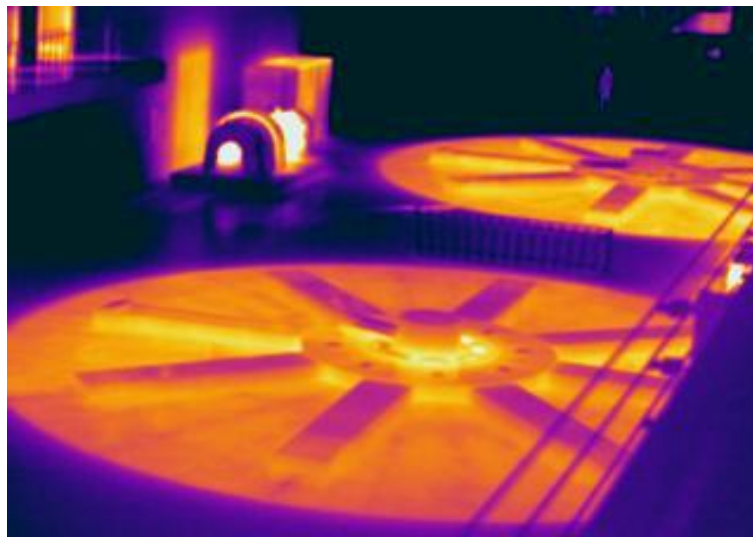


Figure 4.1. IR thermal image of synchronous generators in a power plant.

#### 4.1 The Calorimetric Method

The basic consideration behind the calorimetric method theory is that all of the machine losses are converted into heat. Therefore, if a control volume could be established by involving the machine as shown in Fig. 4.2, all of the machine losses could be determined through the observed heat exchange.

## 4.2 The Calorimetric Method using IR Thermal Imaging

The basic consideration behind the calorimetric method theory is that all of the machine losses are converted into heat. Therefore, if a control volume could be established by involving the machine, as shown in Fig. 4.2, all of the machine losses could be determined through the observed heat exchange.

In this picture, the heat flow of the coolant fluids such as air, water, and oil are depicted along with their input and output temperatures. Radiation and convection heat flow are also shown.

This idea has practical application if such control volume could really be constructed around the machine making it more appropriate for that with small dimensions [4.3-4.4].

For large machines, it becomes easier if the heat transfer is calculated separately for each machine component. The losses are proportional to the increase in temperature of coolant fluids such as air and water for the machine's internal parts, and oil for the bearings. The heat that flows through the machine surface to the concrete and to the environment should also be accounted for. Such a technique is suggested by the standards [18-19] and is described as follows.

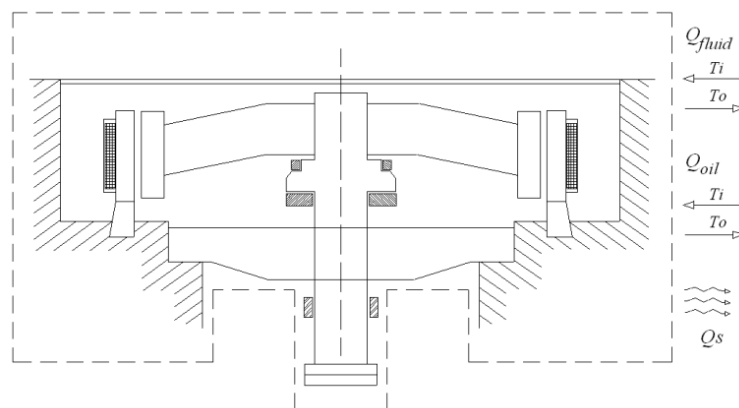


Figure 4.2. Control volume around the electrical machine.

### 4.2.1 Losses absorbed by coolant fluids

This parcel of the losses regards cooled machines, including their parts, in which the moving medium circulates in a closed system. The machine losses absorbed by coolant fluids can be determined using (4.3).

$$P_l = c \rho Q \Delta\theta \quad (4.3)$$

Where  $P_l$  is the calculated absorbed losses (kW),  $c$ ,  $\rho$ ,  $Q$ , and  $\Delta\theta$  are quantities related to the coolant fluid, being its specific heat capacity (kJ/kgK), density (kg/m<sup>3</sup>), volumetric flow (m<sup>3</sup>/s), and temperature rise (K), respectively.

Equation (3.3) can be applied to any coolant fluid on any machine part. The values of specific heat and density should be taken for the average working temperature. Typical values for the most common coolant fluids are presented in Table 3.1.

In general, for air/water cooled machines, the losses determined with this technique are internal losses and include the losses due to the Joule effect on the machine conductors, hysteresis and eddy current losses on the machine core, stray load loss, and friction and windage losses. For separated oil-cooled bearings, the losses in trust and in guide bearings can also be determined by using the same approach and related constants. Examples of measurements are presented in Fig. 4.3 and Fig. 4.4.

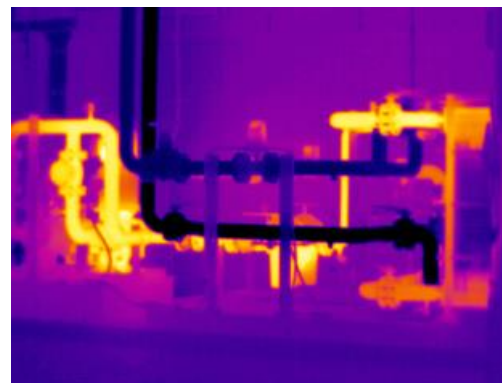
The coolant fluid volumetric flow can be obtained in many ways. Non-intrusive ultrasonic flowmeters have been widely employed with great success due to their improved accuracy and easy application.

Table 4.1. Typical constant values (@ 300K)

Fluid	Air	Water	Oil
$c$ (kJ/kg·K)	1.012	4.181	2.762
$\rho$ (kg/m <sup>3</sup> )	1.184	997.7	876.1



(a)



(b)

Figure 4.3. Combined bearing heat exchanger (a) and thermal image (b).



(a)



(b)

Figure 4.4. IR thermal images from the machine oil-cooled bearings.

#### 4.2.2 Losses released by radiation, convection, and conduction

The heat lost because of radiation and convection may be particularly important in small machines or in large machines having a relatively large amount of exposed surface with operating temperatures appreciably above ambient [4.9].

These losses comprise the heat transfer from the machine surface to the environment, heat transfer to the concrete case, and heat transfer through the machine shaft. The general equation of the radiation and convection losses is:

$$P_l = h A \Delta\theta \quad (4.4)$$

Where  $h$  is the heat transfer coefficient ( $\text{W}/\text{m}^2\cdot\text{K}$ ),  $A$  is the area of the radiant surface ( $\text{m}^2$ ) and  $\Delta\theta$  is the temperature difference between the surface and the environment (K).

While IEEE std-115 suggests 12.4 as the value for  $h$  [4.1], the IEC 34-2 standard considers a value of 15 in the absence of fluid flow [4.2]. Otherwise, a heat transfer coefficient dependent on the coolant fluid speed is specified as follows [4.10].

$$h = 11 + 3 v \quad (4.5)$$

$$h = 5 + 3 v \quad (4.6)$$

Equations (4.5) and (4.6) are suitable for external and internal surfaces, respectively, where  $v$  is the coolant fluid velocity (m/s). Despite the most common standards present, their suggestion regards the heat transfer coefficient determination; a deeper study unveils more suitable ways to determine its value for specific applications and in order to increase the accuracy of the obtained results. In addition, new technologies for surface temperature measurement employing infrared thermal imagers bring new insights for the calorimetric method application and determination of surface losses presented as follows.

#### 4.2.3 Heat Transfer Coefficient

The heat transfer coefficient depends on several physical characteristics such as surface geometry, fluid viscosity, flow velocity, thermal properties, and is given by (4.7) [4.11-4.12].

$$h = \frac{k \text{Nu}}{L} \quad (4.7)$$

Where  $k$  is the fluid thermal conductivity of about 0.0271 ( $\text{W}/\text{m K}$ ) for the air,  $L$  is the equivalent length (m) defined by the area of a surface over its perimeter, and  $\text{Nu}$  is the Nusselt number.

The Nusselt number is the convective to the conductive heat transfer coefficients ratio, and it is a function of the Grashof number (Gr) and the Prandtl number (Pr) product.

$$Nu = a (Gr Pr)^b \quad (4.8)$$

The values of the coefficients a and b depend on the studied object surface and on the product value between the Grashof number and the Prandtl. Typical coefficient values are summarized in Table 4.2.

Table 4.2. Typical values of a and b.

Studied object	a	b	Working range
Horizontal plane surface with hotter upper side	0.54	0.55	$10^4 \leq Gr Pr \leq 10^9$
	0.14	0.33	$10^9 \leq Gr Pr \leq 10^{13}$
Horizontal plane surface with hotter lower side	0.58	0.20	$10^5 \leq Gr Pr \leq 10^{11}$
Horizontal cylinder	0.53	0.25	$10^4 \leq Gr Pr \leq 10^9$
	0.13	0.33	$10^9 \leq Gr Pr \leq 10^{13}$
Vertical surface or vertical cylinder	0.59	0.25	$10^4 \leq Gr Pr \leq 10^9$
	0.10	0.33	$10^9 \leq Gr Pr \leq 10^{13}$

Whilst the Prandtl number remains in the interval 0.7-0.8 for the air, the Grashof number is given by (4.9).

$$Gr = \frac{g L^3 \Delta\theta}{\nu^2 \bar{\theta}} \quad (4.9)$$

Where g is the gravitational acceleration ( $m/s^2$ ),  $\nu$  is the fluid kinematic viscosity considered as  $16.96 \cdot 10^{-6}$  ( $m^2/s$ ) for the air and  $\Delta\theta$  and  $\bar{\theta}$  represent, respectively, the difference and the average temperatures (K) between the surface and ambient.

A calculation example of an actual generator with 13.8 m diameter, surface temperature of 46 °C and ambient temperature of 32 °C would lead to a heat transfer coefficient of 1.95 W/m<sup>2</sup>·K. The IEEE-STD-115 suggested value (12.4) is 6.4 times higher than this value, while the IEC-60034-2-2 standard suggested value (15) is 7.7 times higher than this value.

Such differences can be explained as some authors consider the surface losses as the summation of the radiation and convection losses [15-16]. This fact is also mentioned by the IEEE-STD-115. The radiation losses are given by

$$P_{rad} = \varepsilon \sigma A (\theta_S^4 - \theta_A^4). \quad (4.10)$$

Where  $\varepsilon$  is the surface emissivity,  $\sigma$  is the Stefan-Boltzmann constant equal to  $5.67 \cdot 10^{-8} \text{ W/m}^2\text{K}$ ,  $\theta_S$  and  $\theta_A$  is the surface and ambient temperature (K), respectively. Rearranging,

$$(\theta_S^4 - \theta_A^4) = (\theta_S + \theta_A)(\theta_S^2 + \theta_A^2)(\theta_S - \theta_A). \quad (4.11)$$

Therefore, the radiation losses ( $P_r$ ) can be determined using the same equation used in calculating the convection losses.

$$P_r = h_r A \Delta\theta. \quad (4.12)$$

With  $h_r$  given by:

$$h_r = \varepsilon \sigma (\theta_S + \theta_A) (\theta_S^2 + \theta_A^2) \quad (4.13)$$

Finally, the total losses released by radiation, convection and conduction can be calculated using a composed heat transfer coefficient,  $h'$ , given by

$$h' = \frac{k \text{Nu}}{L} + \varepsilon \sigma (\theta_S + \theta_A) (\theta_S^2 + \theta_A^2) \quad (4.14)$$

The total loss released by radiation, convection, and conduction is:

$$P_l = h' A \Delta\theta \quad (4.15)$$

In recalculating the heat transfer coefficient for the previous example, the result from an updated heat transfer was a coefficient of  $9.79 \text{ W/m}^2\text{K}$ , which is still 21% lower than the IEEE-STD-115 proposed number and 35% lower than the IEC-60034-2-2.

#### 4.2.4 Temperature Measurement

Surface and coolant fluid temperature measurement is an important subject covered by the main standards regarding loading and efficiency determination [4.1-4.2].

In general, the temperature readings are punctual and performed using temperature sensors such as RTDs or thermocouples. Whilst coolant fluid temperature is obtained from sensors installed in appropriate wells, the temperature information from the generator cover surface is taken from the average of a number of discrete distributed sensors readings.

As long as the temperature gradient on the generator cover surface can lead to significantly different temperatures, a more suitable technique is proposed to precede the surface temperature metering with the usage of IR thermal imagers.

Every object above the absolute zero temperature emits electromagnetic radiation due to its atom and molecule agitation. The greater the agitation degree is, the greater

its temperature will be. According to Stefan-Boltzmann law, the total emitted radiation of a body grows at the fourth power of its absolute temperature [4.13].

$$M = \varepsilon \sigma T^4 \quad (4.16)$$

Where  $M$  is the electromagnetic radiation ( $W/m^2$ ),  $T$  is the absolute temperature (K),  $\varepsilon$  is the object surface emissivity (.) and  $\sigma$  is the Stefan-Boltzmann constant, equal to  $5.6704 \cdot 10^{-8}$  ( $W/m^2K^4$ ).

IR thermal imagers take advantage of this physical principle to measure temperature by detecting the emitted electromagnetic radiation of a heated body. Focal plane array (FPA), a matrix of  $m \times n$  optical sensors, is used to convert the emitted radiation into a temperature mapping.

Employing this technique, temperatures can be measured with very high accuracy and resolutions lower than  $0.1^\circ C$ .

With the temperature distribution map in hand, two approaches are proposed in order to determine the radiation losses.

#### 4.2.4.1 FOV span

The field of view (FOV) of a camera is defined by the aperture angle of its lens, which projects the object image onto the FPA. According to Fig. 4.5, in knowing the FOV value for the two Cartesian directions and the orthogonal distance from the camera to the target object surface, it is possible to determine the object area covered by the thermal image.

$$H = 2 d \tan\left(\frac{FOV_x}{2}\right) \quad (4.17)$$

$$V = 2 d \tan\left(\frac{FOV_y}{2}\right) \quad (4.18)$$

Where  $d$  is the orthogonal distance from the camera to the surface defined by  $H$  and  $V$  dimensions (m),  $FOV_x$  and  $FOV_y$  are the field of view in the directions  $x$  and  $y$  ( $^\circ$ ).

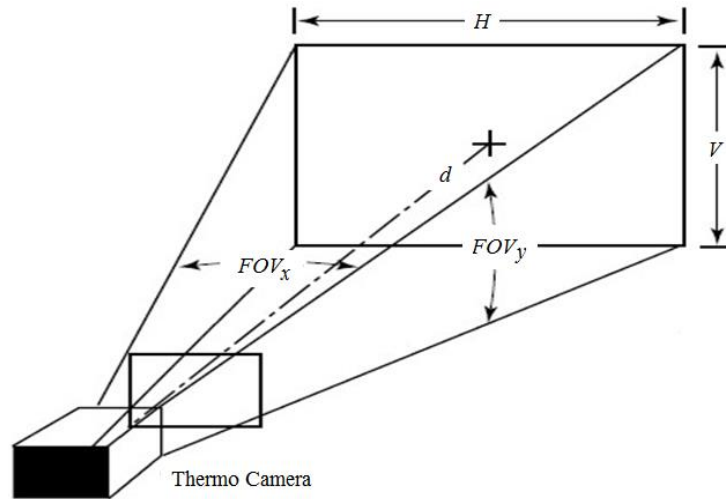


Figure 4.5. Camera FOV and covered area.

The losses along the FOV span area are obtained through the following equation:

$$P_l = h H V \Delta\theta \quad (4.19)$$

Where  $\Delta\theta$  is the average surface temperature increase over the ambient temperature (K).

Equation (4.12) is valid considering a line of sight orthogonal to the plain surface. However, it can be mathematically proven that for a typical FOV lower than  $30^\circ$ , the results remain valid for view angle deviations lower than  $20^\circ$  from the orthogonal.

#### 4.2.4.2 Isotherm diagrams

An alternative proposal for the temperature measurement, along with the determination of the related area, is the segmentation of the whole thermal surface in isotherms.

The isotherm technique consists of establishing a temperature range and of mapping in the original thermal image of all of the pixels with a temperature within this specified range.

As an example, Fig. 4.6 (a) presents a thermal image of a hydro generator surface, while Fig. 4.6 (b) shows the associated isotherm for temperatures around  $36.2^\circ\text{C}$ .

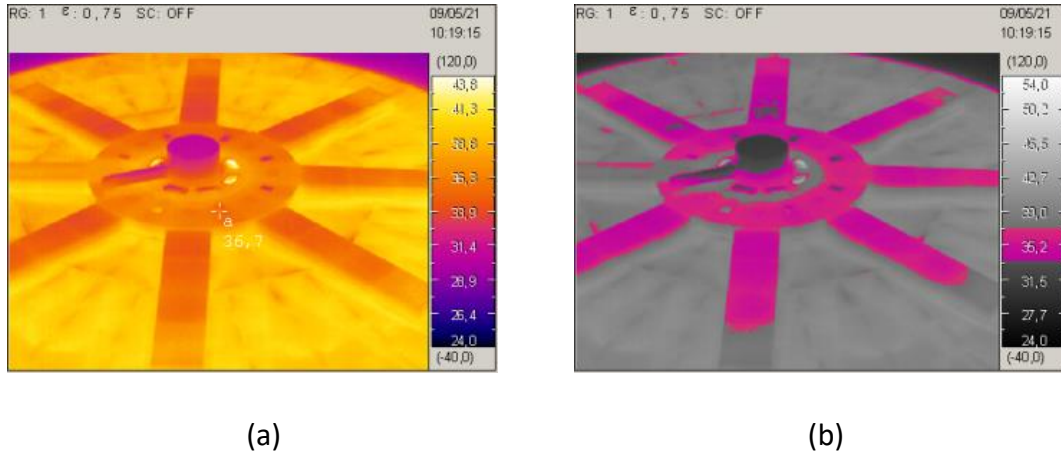


Figure 4.6. IR thermal image and isotherm of the generator cover surface.

The isotherm surface area can be determined in a number of ways. A consistent approach lies in multiplying the number of pixels that satisfies the temperature range criteria by the elementary area covered by each pixel.

This area relates to the instantaneous field of view (IFOV), which is the spatial resolution of the camera ( $^{\circ}$ ), thus defining the smallest detectable target. This depends on the camera FOV and on the FPA resolution. Considering an  $m \times n$  FPA resolution, the equation (4.19) can be rewritten as:

$$P_{\text{losses}} = \frac{H}{m} \frac{V}{n} \sum_{i \in I} N_i h_i \Delta\theta_i \quad (4.20)$$

Where  $I$  denotes the set of considered isotherms.  $N_i$ ,  $h_i$  and  $\Delta\theta_i$  are the number of pixels, the heat transfer coefficient ( $\text{W}/\text{m}^2\text{K}$ ) and the temperature elevation over the ambient temperature ( $\text{K}$ ) for the  $i$ -th considered isotherm, respectively.

#### 4.2.4.3 Loss in the Machine Shaft

An often neglected loss in the main standards is the conductive and convective losses in the machine shaft. Part of the heat created in the shaft friction with the bearing is not extracted by the coolant oil, but rather conducted through the shaft and released into the environment as a convective loss.

Despite its small value, it was easier to neglect this loss than to measure it being as though it was virtually impossible to measure the shaft temperature gradient with the usage of conventional contact temperature sensors.

The advent of IR thermal imagers brought new possibilities of measuring this previously neglected loss. A temperature gradient of more than  $10$  ( $^{\circ}\text{C}$ ) of a hydro generator shaft is shown in Fig. 4.7.

The loss mechanism follows the same theory that is described by equations (4.19) and (4.20). Nevertheless, a different approach must be adopted in order to determine the Nusselt number for a spinning shaft [4.14-4.16].

$$Nu = 0.133 \left( \frac{\omega D^2}{2 \nu} \right)^{0.66} Pr^{0.33} \quad (4.21)$$

Where  $\omega$  is the angular speed (rad/s) and  $D$  is the shaft diameter (m). The length of the shaft shall be used when applying (3.20) during  $h$  calculation.



Figure 4.7. IR thermal image of a generator shaft.

### 4.3 Loss segregation

The different type of losses can be determined using the thermodynamic method. For this reason, running the generator at different conditions, along with applying the presented methodology, will allow for determining the several losses according to their nature.

All of the measurements must be made after reaching thermal equilibrium in which the temperature variation is less than 1% over a 2-hour period. In addition, the temperature of the cooling fluid and irradiation surfaces may not vary more than 0.5 °C in three subsequent measurements spaced 30 minutes between each other.

The operating conditions, often called running, may be divided into first, second, and third runnings depicted as follows [4.1-4.2].

#### 4.3.1 First running

In the first running, the machine is run at its rated speed with no excitation and while disconnected from the grid. The machine must be disconnected from the elevating transformer which guarantees the no-load operation.

After reaching thermal equilibrium, the presented method is applied and the measured losses correspond to the so-called no-load losses which comprise only the ventilation loss. The ventilation loss is the summation of the power dissipated in the cooling system and the radiation and convection surfaces, comprising covering, concrete walls and the shaft.

As the rotating speed remains constant, the ventilation loss is considered constant in all loading conditions. Of course there is friction in the bearings that are very small when compared to the full-load friction loss.

#### 4.3.2 Second running

The machine is run at rated speed with sufficient excitation to obtain rated voltage in its terminals, disconnected from the grid, all of which at no-load. The machine must be disconnected from the elevating transformer which guarantees the no-load operation. In this condition there are only the no-load losses and the core losses.

After reaching thermal equilibrium, the total amount of losses is determined using the presented infrared approach. Subtracting the loss obtained in the first running from the losses obtained in the second running will eventually result in the core loss plus the excitation loss.

The excitation loss can be determined from the relation between quantities of excitation (voltage and current), which results in the field resistance, and the squared field current. Therefore, the core loss can be determined.

#### 4.3.3 Third running

The third running is conducted with the machine under permanent three-phase short-circuit and is sufficiently excited in order to obtain a rated armature current, which is enough to determine additional loss and armature copper loss.

After reaching thermal equilibrium, the loss in this test is determined from the summation of the power dissipated in the cooling system and the radiation and convection surfaces, comprising covering, concrete walls and shaft.

The additional loss is determined by subtracting the armature copper loss, field copper loss, and ventilation loss from the total loss measured in this test.

The armature copper loss is determined from the measured resistance corrected with temperature and the armature current of this test. Field loss is determined as the product from the excitation current and voltage. The ventilation loss is that determined in the first running with eventual correction due to density of the air and pressure variations.

## CHAPTER 5

### CAPABILITY CHART OF A GENERATOR

The limit of operation of a synchronous generator is essentially of a thermal nature. The current flowing in the windings results in a temperature increase and in machine heating. Of course, the machine is designed to afford this temperature rise provided that it works in an admissible region. The capability chart delimits a region in the geometric locus of active and reactive power planes where the machine can work freely without trespassing temperature limits. References [5.1] to [5.5] bring forth excellent information regarding how to draw the capability chart, including the step-up transformer [5.6].

As long as the capability chart delimits the freedom of operation, it is included in the main power system simulator software [5.7-5.8], including AVR and their limiters [5.9-5.11]. Protection studies also consider the capability curve and assure that the machine will work in the allowed region [5.12-5.13]. The extent of the influence of saturation in the capability chart, proven through field tests, has been demonstrated [5.14-5.17]. The influence of operating conditions and the development of the capability chart starts from the construction of phasor diagrams.

#### 5.1 Phasor diagram

The phasor diagram is a geometrical construction that aims at representing electrical quantities as sinusoids of the same frequency. For instance, consider a voltage described by the following expression:

$$v = \sqrt{2} V \sin(\omega t - \Phi) \quad (5.1)$$

In this expression,  $v$  is the instantaneous value of voltage,  $V$  is the effective value of the voltage,  $\omega$  is the angular speed ( $2\pi f$ ) and  $\Phi$  is the displacement angle of the voltage in relation to a rotating reference ( $\omega t$ ). Using such definitions, it is possible to construct the phasor diagram depicted in Fig. 5.1

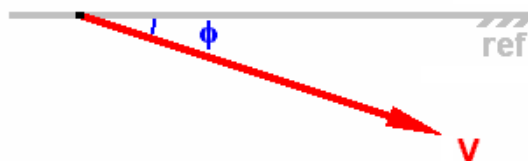


Figure 5.1. Phasor diagram.

Consider the following model to represent a generator connect to any load.

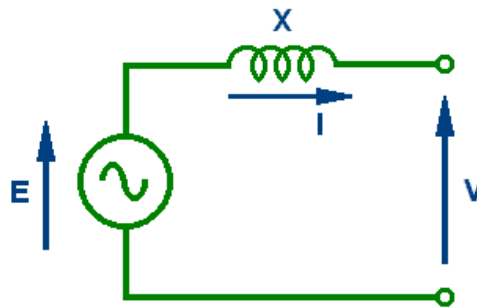


Figure 5.2. Electric diagram.

In Fig. 5.2,  $E$  is the induced voltage,  $V$  is the terminal voltage,  $X$  represents the machine reactance and  $I$  is the load current. For an inductive load, and taking the terminal voltage as a reference, the following expression may be written.

$$E = V + j X I \quad (5.2)$$

In phasor form, the (5.2) may be like Fig. 5.3.

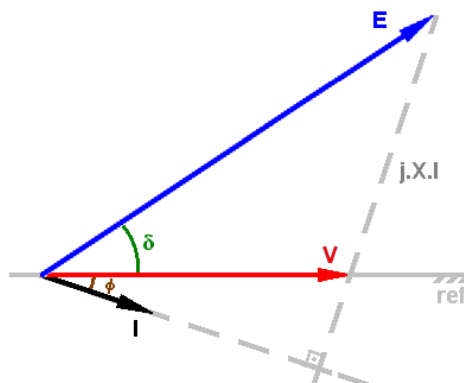


Figure 5.3. Phasor diagram.

For the first time, the  $\delta$  angle appears in this diagram. This angle is often referred to as the loading angle or power angle. This is not the load angle that conducts the load power factor, but rather the angle between induced and terminal voltages. The induced voltage is attached to the rotor. Therefore, the loading angle also defines the position or the pole when a lag of 90 degrees between the induced voltage and the pole windings is considered.

The synchronous machine is represented as a reactance behind a power supply model, which is only valid for machines with cylindrical rotors as long as the reluctance of a round rotor generator is almost the same regardless of the direction taken. Nevertheless, this does not happen with salient pole machines so long as the

reluctance is much smaller in the pole shoe region (direct axis) than in the between poles (quadrature axis), which gives origin to two different types of reactance: the direct axis reactance and the quadrature axis reactance.

In general, the quadrature axis reactance ( $X_q$ ) is of the order of 65% to 85% of the direct axis reactance ( $X_d$ ) in salient pole machines whereas for round rotor machines, the quadrature axis reactance is of the order of 92% to 98% of the direct axis reactance. Normally, for round rotor machines, it is considered that  $X_q$  is equal to  $X_d$ , as the most considered testing standards allow an error of 10% in synchronous parameter determination. Considering that  $X_q$  is equal to  $X_d$ , adhering to a maximum error of 8%, which is lower than the error is allowed by testing standards.

The decomposition of the load current in components according to the direct axis and quadrature axis results in (5.3) which is the expression of the induced voltage in salient pole machines.

$$E = V + j X_d I_d + j X_q I_q \quad (5.3)$$

In phasor form:

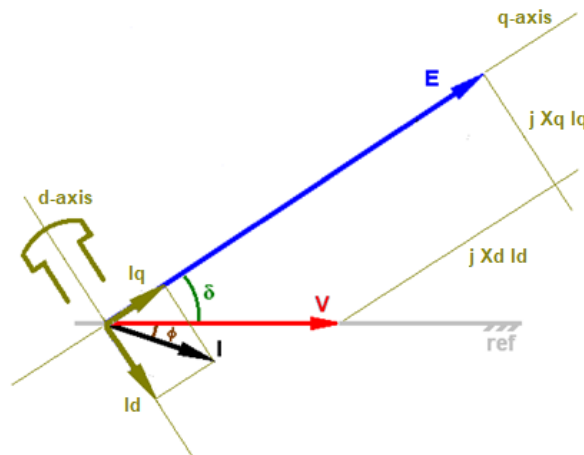


Figure 5.4. Phasor diagram for round rotor synchronous machines.

However, it is hard to obtain the previous phasor diagram as long as the locations of the d-axis and of the q-axis are unknown. Therefore, a mathematical artifice is used, adding and subtracting  $j X_q I_d$  in 5.3, resulting in the following:

$$E = V + j X_d I_d + j X_q I_q + j X_q I_d - j X_q I_d$$

$$E = V + j X_q I + j (X_d - X_q) I_d \quad (5.4)$$

The following phasor diagram can be obtained.

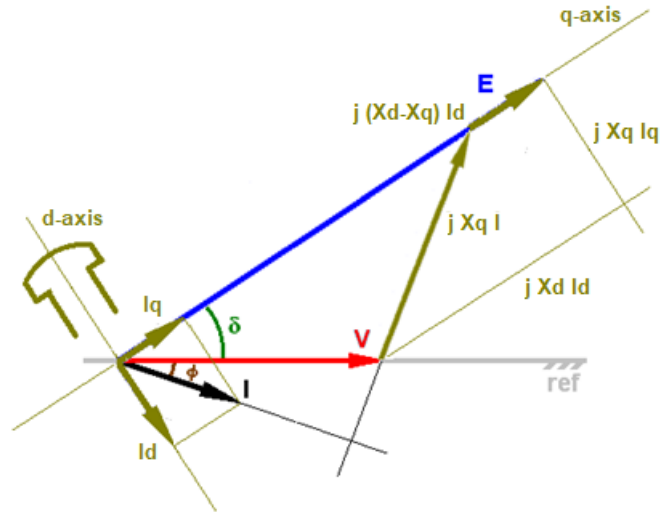


Figure 5.5. Phasor diagram for salient pole synchronous machines.

## 5.2 Steady-state operation

The operation of a synchronous generator at the steady state consists of the control of the effective value and of the frequency of the terminal voltage when out of synchronism. In addition to this, it dispatches the active and reactive powers when connected to the grid. In an off-grid operation, the generated voltage frequency will follow the speed of the prime mover while the voltage effective value is a direct function of the excitation current. Both speed and excitation are respectively controlled by the speed governor and voltage regulator.

When the machine operating is connected to a power system considered as an infinite bus, both the frequency and voltage are defined by the power system. In this case, the speed governor and the voltage regulator miss their original aims and are now responsible for the active and reactive power dispatch. The following table presents the functions of the regulator under each condition.

Table 5.1. Regulator's function.

Studied object	On Grid	Off Grid
Speed Governor	Active Power	Speed, frequency
Voltage Regulator	Reactive Power	Voltage value

For a salient pole machine, the generated active and reactive powers may be calculated by using (5.5) and (5.6) respectively.

$$P = \frac{E V}{X_d} \sin(\delta) + \frac{V^2}{2} \left( \frac{1}{X_d} - \frac{1}{X_q} \right) \sin(2\delta) \quad (5.5)$$

$$Q = \frac{E V}{X_d} \cos(\delta) - V^2 \left[ \frac{\sin^2(\delta)}{X_d} + \frac{\cos^2(\delta)}{X_q} \right] \quad (5.6)$$

In these expressions, P is the active power (W), Q is the reactive power (var), E is the induced voltage (V) and V is the terminal voltage (V).

A simplification of the previous equations considers the inexistence of the rotor saliency, conducting to a cylindrical rotor and resulting in a quadrature axis reactance equal to the direct axis reactance. In this case, the following equations are reached:

$$P = \frac{E V}{X_d} \sin(\delta) \quad (5.7)$$

$$Q = \frac{E V}{X_d} \cos(\delta) - \frac{V^2}{X_d} \quad (5.8)$$

### 5.3 P- $\delta$ diagram

According to (5.5) and (5.7), the generated active power is strongly dependent on the power angle and less dependent on the induced voltage. On the other hand, the reactive power is less dependent on the power angle and is strongly dependent on the induced voltage as can be seen in (5.6) and (5.8). It may be explained by the fact that the sin function has a big derivate close to zero whereas the opposite can be observed for a cosine function.

Also, as seen in (5.7), the maximum power transfer in a turbo-generator happens when the loading angle is  $90^\circ$ . Beyond this angle, an increase in the loading angle, aiming at a generation increase results in the opposite, thus reducing the power and igniting an instability process. Therefore, for round rotor machines,  $90^\circ$  is the theoretical stability limit as depicted in Fig. 5.6.

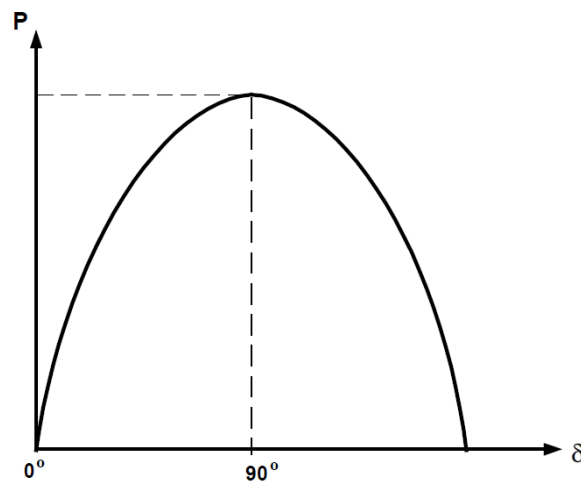


Figure 5.6. P- $\delta$  diagram for a round rotor synchronous machine.

For a salient pole machine, the  $P-\delta$  diagram is that shown in Fig. 5.7. As can be seen in (5.5), there is a second harmonic component that must be added to the fundamental component. This second harmonic is often called “reluctance power” and is due to the reluctance difference, resulting in different types of reactance ( $X_q/X_d$ ) for salient pole machines. The theoretical stability limit is therefore in a given angle less than  $90^\circ$ .

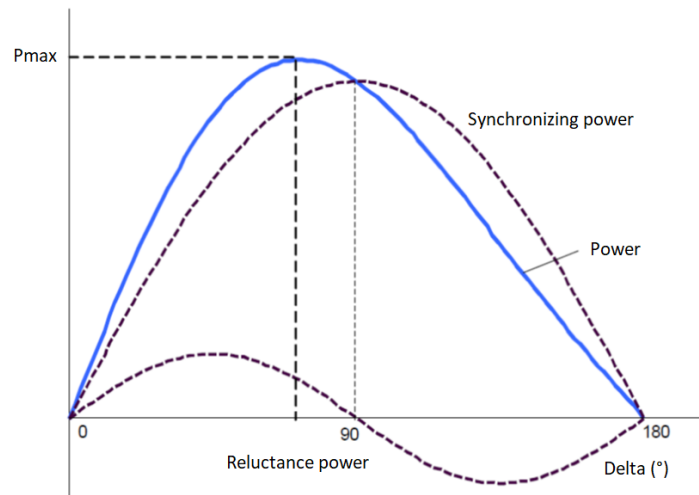


Figure 5.7.  $P-\delta$  diagram for a salient pole synchronous machine.

#### 5.4 Capability chart

The most severe operative limitations of a given machine are thermal limits, which may be due to currents flowing in the machine windings or due to circulation of eddy currents in the magnetic core of the armature. Thus, the capability chart is the geometric locus in the active and reactive power plane where the machine can have free operation without hurting temperature limits. Stability is an additional limit that must be accounted for.

Figure 5.8 shows a hypothetical capability chart for a salient pole synchronous machine where the limitations are highlighted. The portion A-B is the field heating limit and is defined by the rated armature current and rated power factor. B-C is the armature heating limit defined by the rated apparent power which is proportional to the rated armature current; C-D is the practical stability limit obtained from the theoretical stability limit; D-E is the minimum field current and is defined by the residual magnetism of the machine.

Other not shown applicable limits are imposed by the voltage regulator operation, namely the maximum and minimum operating limits of the prime mover, maximum and minimum limits of the terminal voltage, minimum excitation, and others.

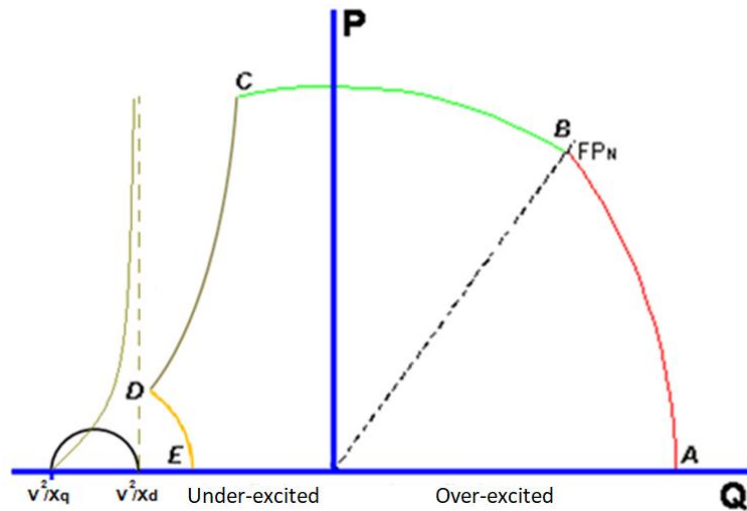


Figure 5.8. Capability chart for a salient pole synchronous machine.

Figure 5.9 shows the capability chart of a round rotor synchronous machine. The parts A-B and B-C of this chart are quite equal to the capability chart of a salient pole synchronous machine. The difference is that the saliency is neglected and  $X_q$  becomes equal to  $X_d$ . Therefore, the semi-circle reduces itself to a single point. This figure also presents the armature core end heating limit described by the part C-D, which is proper of rounded rotor machines and neglected for salient pole machines.

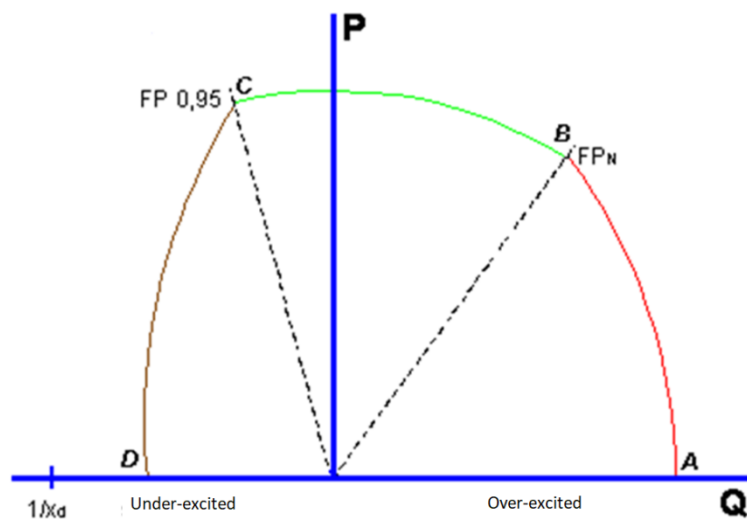


Figure 5.9. Capability chart for a rounded rotor synchronous machine.

The long-term loading beyond these limits ought to cause overheating and useful life-time reduction and must be avoided. Nonetheless, a time-limited short-duration overloading may be allowed with no compromising of the insulation, given by:

$$t = \frac{k}{I^2 - 1} \quad (5.9)$$

Where  $t$  is the limited time overloading (s),  $I$  is the overloading current (pu) and  $k$  is a number between 100 and 250 given by the manufacturer [5.18-5.20].

#### 5.4.1 Capability construction

For a rounded rotor synchronous machine, multiplying all of the lengths of the phasor diagram of Fig. 5.3 by  $V/X_d$  will result in the power triangle as depicted in Fig. 5.10 that can be obtained.

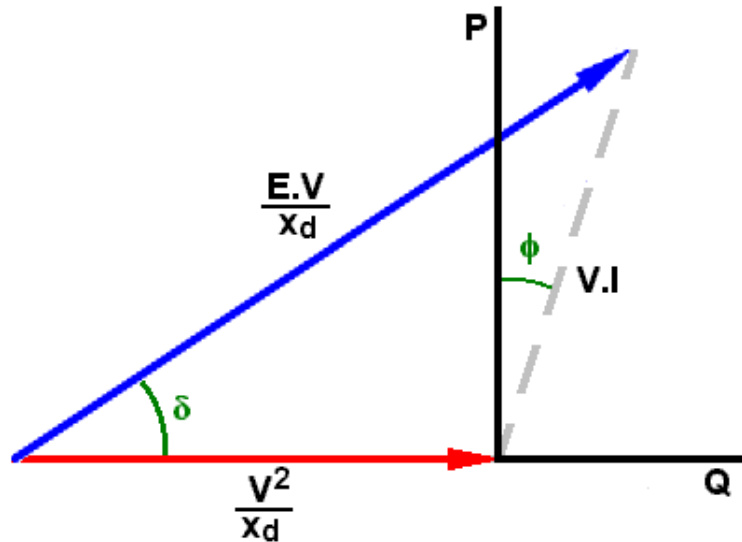


Figure 5.10. Modified phasor diagram.

Neglecting the saturation, the side  $EV/X_d$  is proportional to the excitation current as  $E$  is a direct function of the excitation current. The rated field current is related to rated induced voltage and is considered as a limitation for the heating of the field windings. On the other hand,  $VI$  is proportional to the apparent power and to the armature current, giving a good indication of the armature current limit for rated conditions.

As explained, for a round rotor synchronous machine, the maximum power transfer occurs when the loading angle is  $90^\circ$  in which it establishes the theoretical stability limit. The practical stability limit is obtained by applying a safety factor either over the loading angle or over the active power for the same excitation. For the complete capability chart of the round rotor machine, the minimal excitation limit must be added, which is about 10-15% of the rated field current and is depicted in Fig. 5.11.

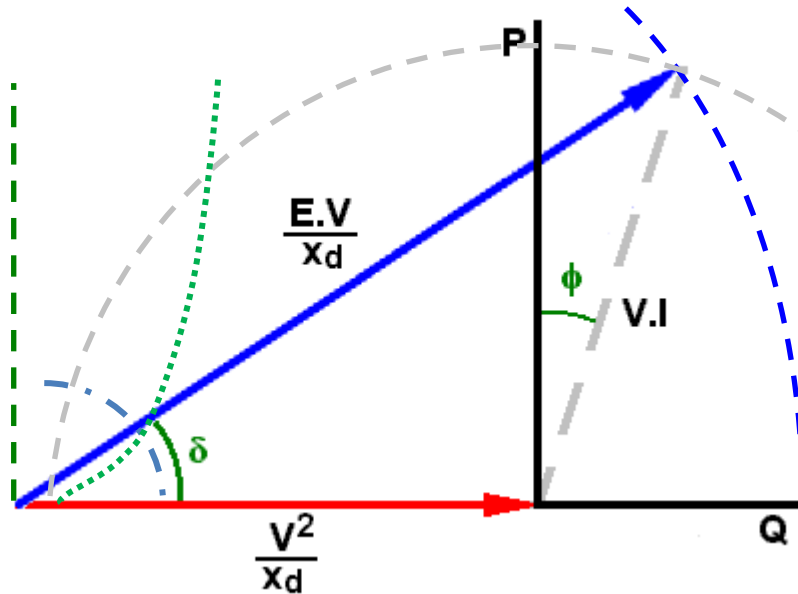


Figure 5.11. Limits construction of a capability chart for a round rotor synchronous machine.

On the other hand, for rounded rotor synchronous machines, there are much more limiting factors than the practical stability limit or the minimum excitation limit, which must also be accounted for. This is the armature core end heating limit [5.21-5.24]. The armature core end heating happens when, under field weakness, the flux lines enter the magnetic circuit orthogonally with the lamination of the core. Large currents are induced in the laminations resulting in heating, as depicted in Fig. 5.12.

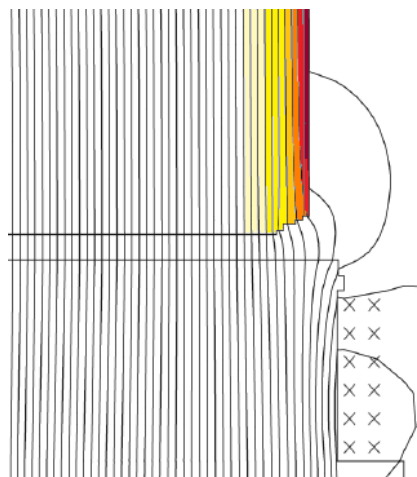


Figure 5.12. Operation under flux weakness condition.

This limit is firstly defined in the V chart of the machine (the curves that relates the armature current to the field current) and then transposed to the capability chart. A limiting straight line is drawn between two points in the V chart. The first point is defined by 75% of the rated armature current and 25% of the rated excitation current. The second point is defined by 100% of the rated armature current and the rated power factor; the related field current is then determined as depicted in Fig. 5.13.

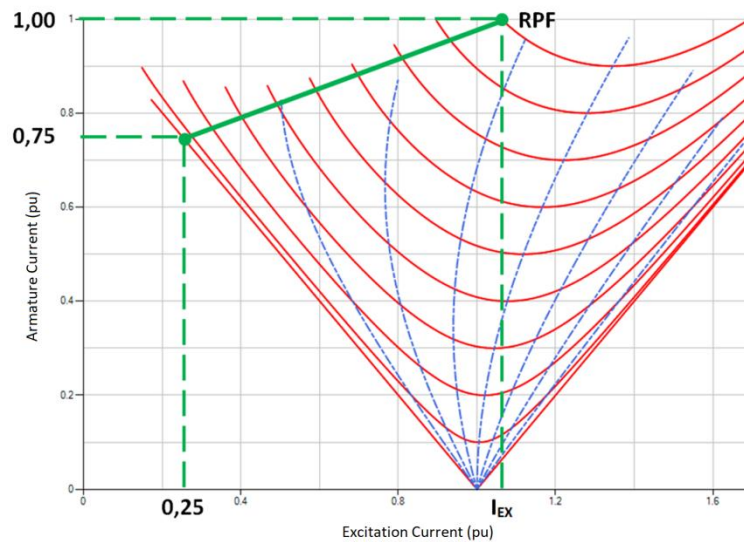


Figure 5.13. V-curve and armature core-end heating limits construction.

The values obtained in this straight line must be translated to the P-Q plane, resulting in the core-end heating limit. This limit is prominent in cylindrical rotor machines even though it can show-up in salient-pole machines. In order to minimize such a problem, it is common to produce the armature in a leader shape as shown in Fig. 5.14 while avoiding the ending of flux lines in the lamination plane of the armature core.

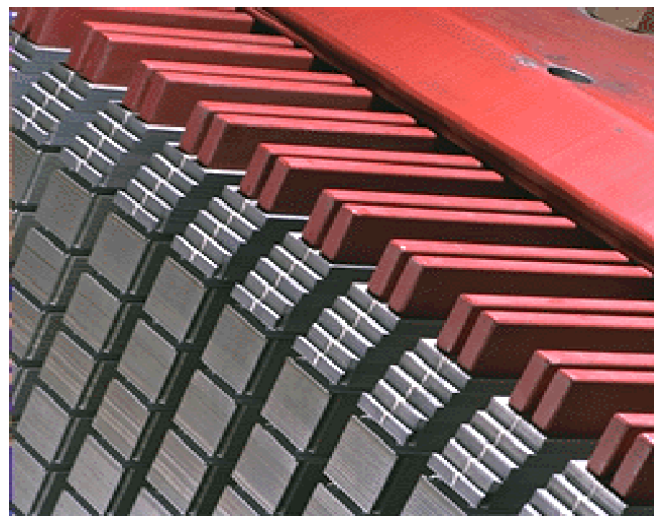


Figure 5.14. Modified laminations to reduce the effects of transversal fluxes.

Due to saliency, the construction of the capability chart for salient-pole synchronous machines needs a modification in the phasor diagram of Fig. 5.5, thus obtaining the diagram of the Fig. 5.15.

The triangle inserted in the semi-circumference is by definition a rectangle. The smaller leg,  $(X_d - X_q) I_q$ , is proportional to the terminal voltage projection into the quadrature axis,  $V \sin(\delta)$ . As  $I_q$  is  $V_q/X_q$ , the hypotenuse, or the diameter of the circumference is  $V(X_q - X_d)/X_q$ .

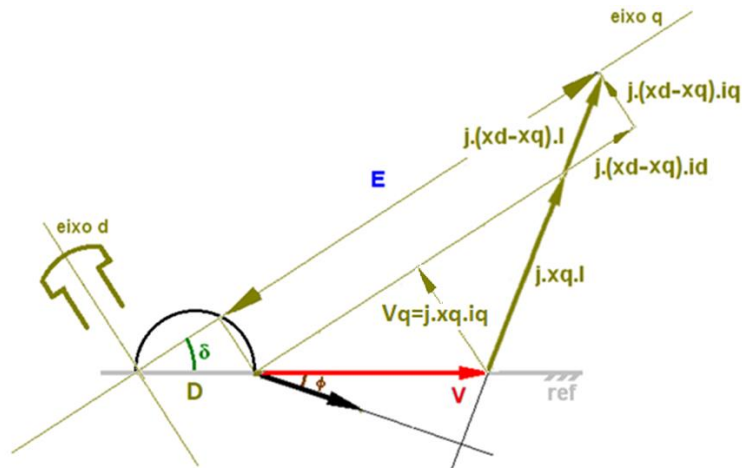


Figure 5.15. Phasor diagram for salient pole synchronous machine.

Due to saliency, the construction of the capability chart for salient-pole synchronous machines needs a modification in the phasor diagram of Fig. 5.5, thus obtaining the diagram of the Fig. 5.15.

Again, multiplying the sides by  $V/X_d$  will result in a power diagram. The extreme coordinates of the semi-circumference will be  $V^2/X_q$  and  $V^2/X_d$ . Following the same steps taken in the case of rounded-rotor synchronous machine, there will be a power diagram with limits shown in Fig. 5.16.

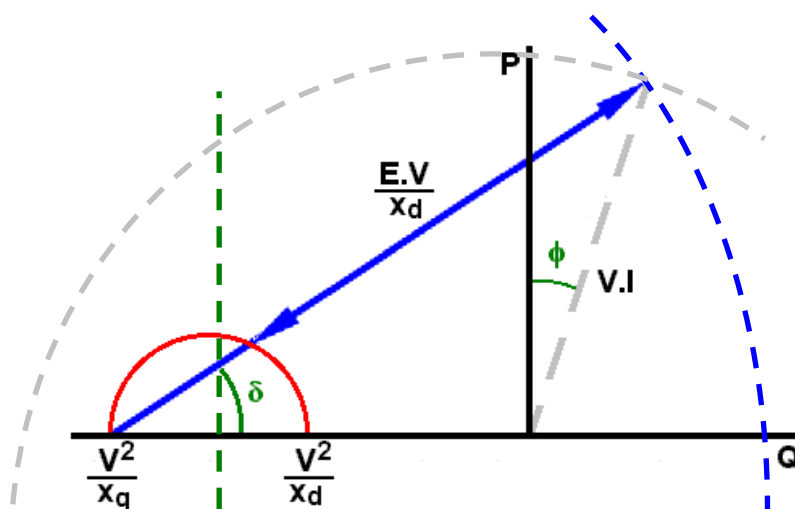


Figure 5.16. Introduction of limits.

As in the rounded-rotor synchronous machine, the curve A-B is the field heating limit and is defined by the heating created by the rated field current. It is constructed by using several radial lines departing from  $V^2/X_q$ . The semi-circumference with a diameter of  $V^2/X_q - V^2/X_d$  can be considered. In doing so, one can note that as the unique radial line that comes out of  $V^2/X_q$  and passes through the point defined by the rated armature current at a rated power factor, the rated field current is proportional to the length that departs from the semi-circumference border and ends-up on this point.

The field heating limit curve is constructed by repeating this length in the several radial lines. The curve B-C is the armature heating limit, defined by a circle centered in the origin of the diagram and radius equal to the armature rated current. In per unit size, this radius is equal to one. C-D is the practical stability limit, and D-E is a minimum field current.

In (5.5) one can observe that theoretically, the maximum power transfer happens in an angle that is less than  $90^\circ$ . This is the theoretical stability limit. As in the round-rotor synchronous machine, the practical stability limit is obtained by applying a safety factor either over the loading angle or over the active power under a given excitation. Adopting the first approach, the maximum power for a given loading angle is given from the partial derivative (5.5) with respect to the loading angle, and making it equal to zero, resulting in 5.10.

$$\frac{\partial P}{\partial \delta} = \frac{E V}{X_d} \cos(\delta) - V^2 \left( \frac{1}{X_d} - \frac{1}{X_q} \right) \cos(2\delta) = 0 \quad (5.10)$$

While the diagram P-  $\delta$  relates the generated power to the loading angle, it may be constructed with the available induced voltage. In order to have the maximum power, the induced voltage is obtained from the later equation and is given by:

$$E = V \left( 1 - \frac{X_d}{X_q} \right) \frac{\cos(2\delta)}{\cos(\delta)} \quad (5.11)$$

There are two approaches to define the practical stability limit. The first is to consider a constant excitation voltage while allowing a safety factor, for instance 0.75, over the loading angle for which a new induced voltage is calculated. The second approach is to calculate the loading angle using (5.10). The following trigonometric identity is used:

$$\cos(2\delta) = 2 \cos^2(\delta) - 1 \quad (5.12)$$

Resulting in (5.13).

$$2 V^2 \left( \frac{1}{X_d} - \frac{1}{X_q} \right) \cos^2(\delta) + \frac{E V}{X_d} \cos(\delta) - V^2 \left( \frac{1}{X_d} - \frac{1}{X_q} \right) = 0 \quad (5.13)$$

Dummy variables are used.

$$p = \cos(\delta) \quad (5.14)$$

$$a = 2 V^2 \left( \frac{1}{X_d} - \frac{1}{X_q} \right) \quad (5.15)$$

$$b = \frac{E V}{X_d} \cos(\delta) \quad (5.16)$$

$$c = -V^2 \left( \frac{1}{X_d} - \frac{1}{X_q} \right) \quad (5.17)$$

Therefore,

$$a p^2 + b p + c = 0. \quad (5.18)$$

Where  $p$  can be determined as the solution of a second order polynomial.

$$p = \frac{-b + \sqrt{b^2 - 4 a c}}{2 a} \quad (5.19)$$

The corresponding delta angle is the angle in which its cosine is  $p$ .

$$\delta = \arccos(p) \quad (5.20)$$

Therefore, the complete capability chart must consider the minimum excitation limit as seen in Fig. 5.17.

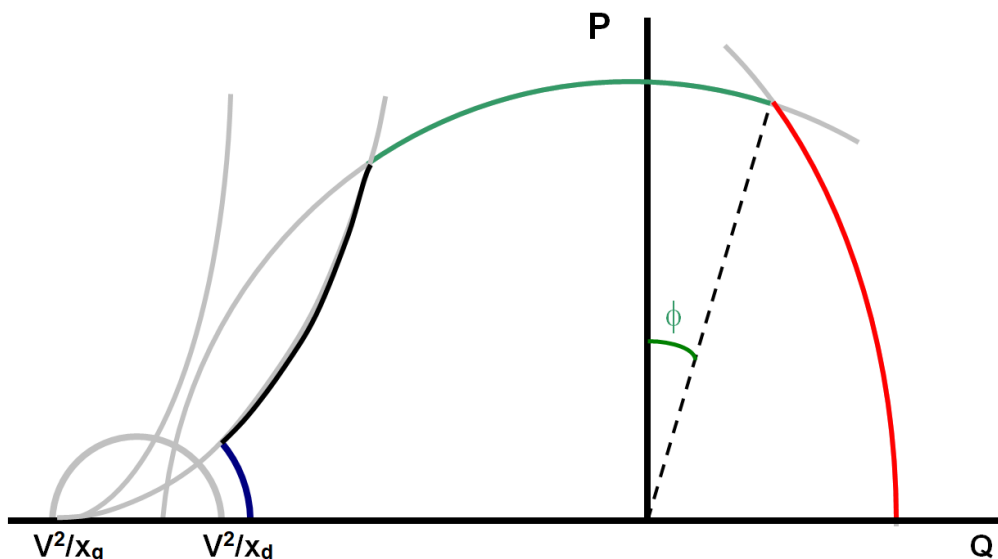


Figure 5.17. Operating limits of a salient-pole synchronous machine.

A complete capability curve, along with its limits, is shown in Fig. 5.18 for a machine with  $X_d=1.15$  and  $X_q=0.8$ .

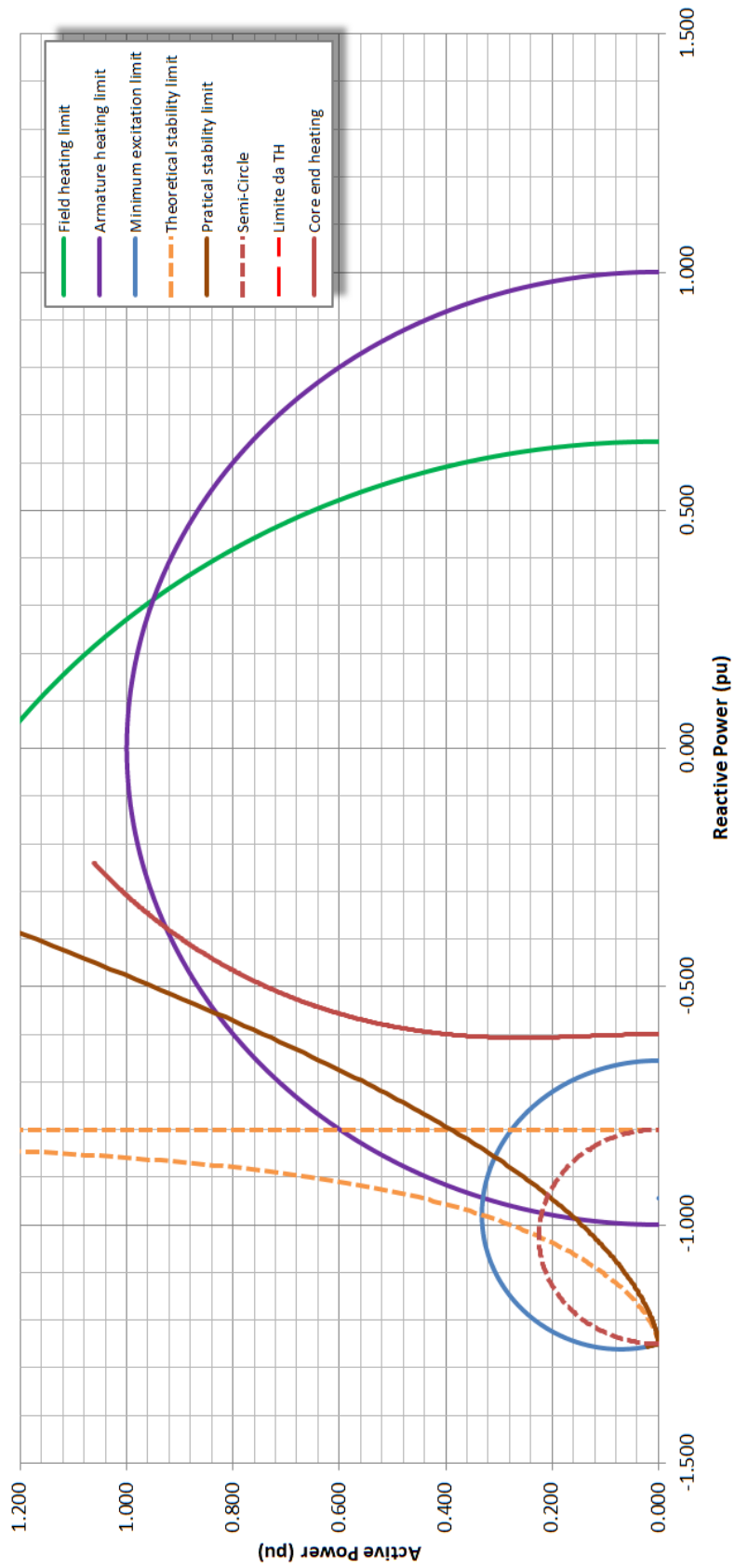


Figure 5.18. Capability curve of a salient-pole synchronous machine.

## CHAPTER 6

### VALIDATION AND APPLICATION TO EXISTENT MACHINES

#### 6.1 Validation of the methodology

The proposed method was validated using two important machines, one from a medium head power plant and other from a low head power plant using bulb generator. The methodology proposed was compared with results from proved software used to design those machines. The main results are presented as follows.

##### 6.1.1 Validation against a large generator

The rated quantities of the generator are presented in Table 6.1 and the calculated losses are presented in Table 6.2.

Table 6.1. Rated quantities

Quantity	Unit	Value
Rated apparent power	MVA	679
Power factor	-	0.9
Rated voltage	kV	18
Rated current	A	21779
Rated speed	rpm	85.7
Runaway speed	rpm	162
Rated frequency	Hz	60
Direct axis reactance ( $X_d$ )	pu	0.98
Quadrature axis reactance ( $X_q$ )	pu	0.69
Potier reactance ( $X_p$ )	pu	0.18

Table 6.2. Rated quantities

Quantity	Unit	Value
Losses in active Iron (core loss @ no load)	kW	1577.8
Brush mechanical friction loss	kW	6.5
Bearing loss	kW	60
Windage loss and viscous friction	kW	2781
$I^2R$ in armature winding DC loss (CC @ 95 °C)	kW	1570.8
$I^2R$ in field winding DC loss (CC @ 95 °C)	kW	1467
All electric losses in excitation system	kW	117.9
Losses introduced by load in active iron	kW	830.9

The no-load saturation curve was obtained and is shown in Fig. 6.1.

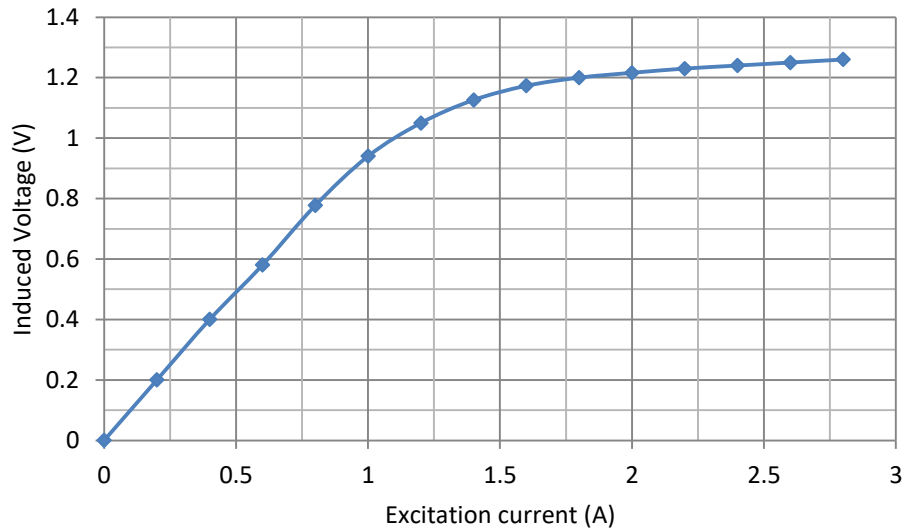


Figure 6.1. Per-unit saturation curve.

All of the presented data were used to obtain the efficiency map of the machine under study. In addition, efficiency points were obtained with the manufacturer applying the same proven software used to design the machine. The comparison of both results can be made from the picture depicted in Fig. 6.2.

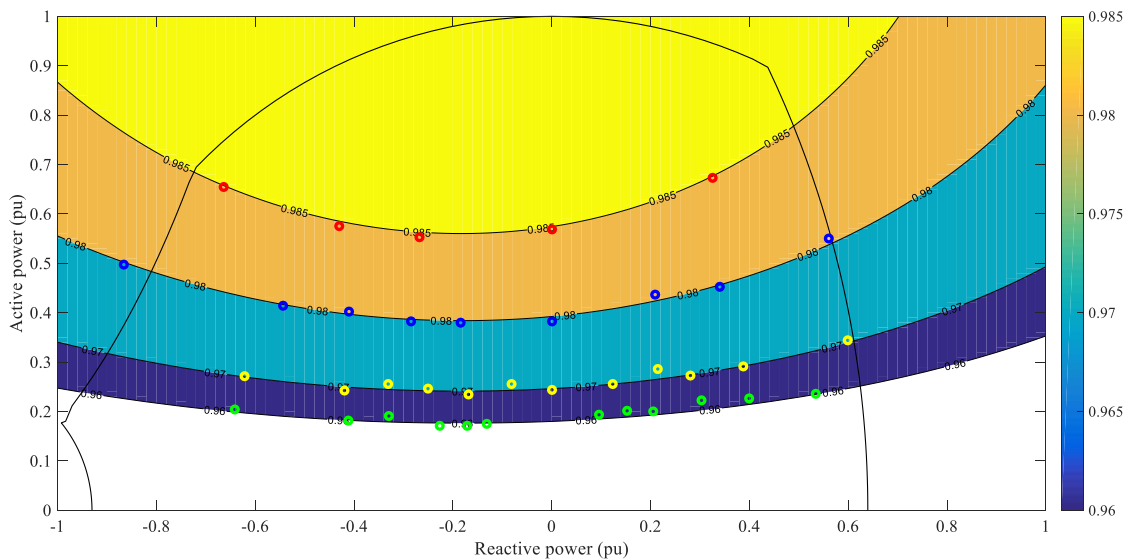


Figure 6.2. Efficiency mapping .

### 6.1.2 Validation against a bulb generator

The rated quantities of the generator are presented in Table 6.3 and the calculated losses are presented in Table 6.4.

Table 6.3. Rated quantities

Quantity	Unit	Value
Rated apparent power	MVA	82.25
Power factor	-	0.9
Rated voltage	kV	13.8
Rated current	A	3441
Rated speed	rpm	100
Runaway speed	rpm	300
Rated frequency	Hz	60
Direct axis reactance ( $X_d$ )	pu	1.09
Quadrature axis reactance ( $X_q$ )	pu	0.72
Potier reactance ( $X_p$ )	pu	0.2

Table 6.4. Rated quantities

Quantity	Unit	Value
Core loss	kW	240.4
Brush loss	kW	2.5
Bearing loss	kW	0
Windage and friction loss	kW	200
Armature winding current loss (@ 95 °C)	kW	425.2
Field winding current loss (@ 95 °C)	kW	286.1
Excitation loss	kW	23.1
Stray-load loss	kW	144.6

The no-load saturation curve was obtained and is shown in Fig. 6.3.

All of the presented data were used to obtain the efficiency map of the machine under study. In addition, efficiency points were obtained with the manufacturer applying the same proven software used to design the machine. The comparison of both results can be made from the picture depicted in Fig. 6.4.

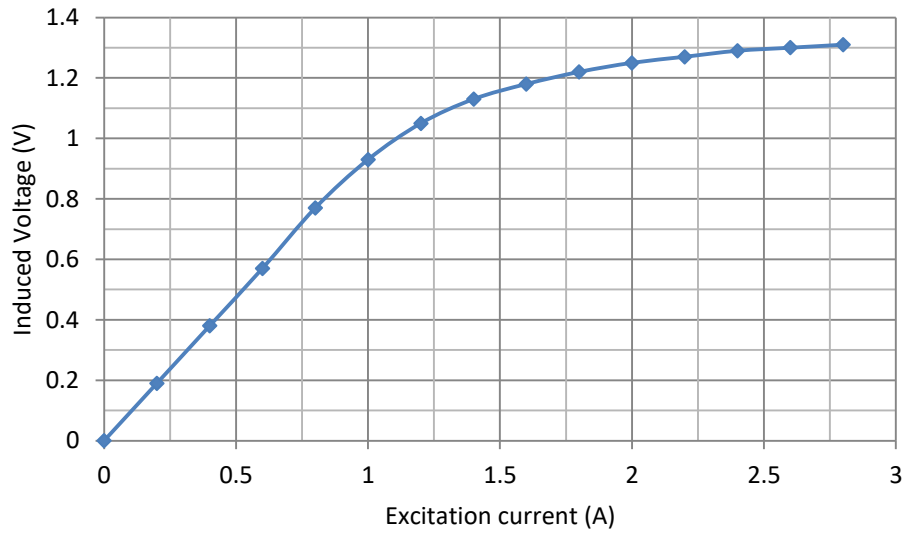


Figure 6.3. Per-unit saturation curve.

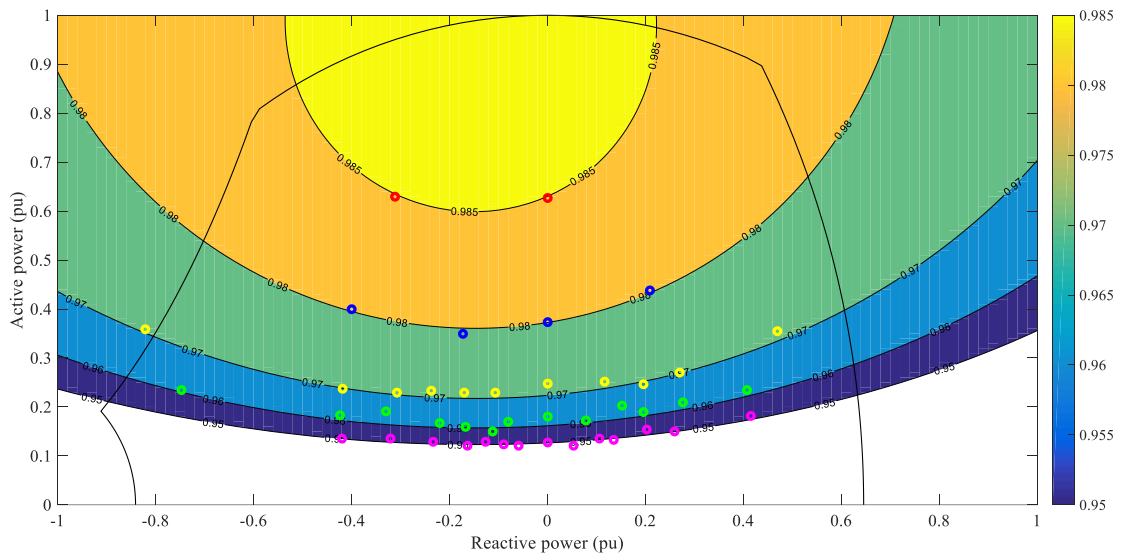


Figure 6.4. Efficiency mapping.

## 6.2 Application to existent machine

The presented procedures were applied to the generator of the unit #6 of Furnas hydropower plant to obtain its weighted average efficiency in order for it to be evaluated. Tests were applied to this machine so as to determine its losses and to evaluate its efficiency throughout all of its operating range. Concomitantly, its usage over an entire year was obtained, giving a basis to evaluate its operating histogram.

The rated quantities of this generator are 150 MVA, 15 kV, PF 0.95.

### 6.2.1 Tests for losses evaluation

The segregated losses were determined using the presented methodology. The results can also be found in report [6.1].

#### A. First running

The first running is applied to the machine at no-load and no-excitation. The presented losses are due strictly to ventilation. The infrared thermodynamic test was applied. The main measured quantities during this test are depicted in Tables 6.5 and 6.6. The tables also present the power loss calculations.

Table 6.5. Loss in the radiator

Symbol	Quantity	Unit	Value
Q	Flow in the radiator	m <sup>3</sup> /s	0.018209
T <sub>i</sub>	Water input temperature	°C	25.861
T <sub>o</sub>	Water output temperature	°C	34.885
ΔT	Temperature difference	°C	9.024
P <sub>1</sub>	Total loss in the radiator	kW	683.683

Table 6.6. Loss within the surfaces

Symbol	Quantity	Unit	Value
P <sub>21</sub>	Loss in the generator covering	kW	18.738
P <sub>22</sub>	Loss in the generator walls	kW	4.154
P <sub>23</sub>	Loss in the turbine covering	kW	3.900
P <sub>2</sub>	Total loss in the surfaces	kW	26.792

Therefore, the total loss in the first running is the summation of the losses in the radiator and in the radiant surfaces, and represents the ventilation losses, which eventually becomes **710.47 kW**. Table 6.7 shows the ambient quantities during the tests used in the calculations.

Table 6.7. Ambient quantities

Symbol	Quantity	Unit	Value
$P_{atm}$	Atmospheric pressure	mbar	935.70
UR	Relative humidity	%	32.76
$T_{amb}$	Temperature	°C	36.371
$\rho_{b0}$	Air density	kg/m <sup>3</sup>	1.135

#### B. Second running

The second running, with the machine at no-load and rated terminal voltage, is applied in order to determine the iron loss.

Table 6.8. Loss in the radiator

Symbol	Quantity	Unit	Value
Q	Flow in the radiator	m <sup>3</sup> /s	0.036686
$T_i$	Water input temperature	°C	25.861
$T_o$	Water output temperature	°C	34.957
$\Delta T$	Temperature difference	°C	9.095
$P_1$	Total loss in the radiator	kW	1388.259

Table 6.9. Loss within the surfaces

Symbol	Quantity	Unit	Value
$P_{21}$	Loss in the generator covering	kW	24.021
$P_{22}$	Loss in the generator walls	kW	9.755
$P_{23}$	Loss in the turbine covering	kW	10.820
$P_2$	Total loss in the surfaces	kW	44.595

The total loss in the first running is the summation of the losses in both the radiator and the radiant surfaces. It represents the core loss plus ventilation loss and the rotor loss.

The rotor copper loss is determined by multiplying the rotor resistance with the square of the excitation current, which is **182.58.47 kW**. Therefore, the core loss is **540.38 kW**. Table 6.6 shows the ambient quantities during the tests.

Table 6.10. Ambient quantities

Symbol	Quantity	Unit	Value
$P_{atm}$	Atmospheric pressure	mbar	935.21
UR	Relative humidity	%	28.76
$T_{amb}$	Temperature	°C	38.529
$\rho_{b0}$	Air density	kg/m <sup>3</sup>	1.133

### C. Third running

The third running is conducted while the machine is in a three-phase short circuit with enough excitation to obtain a rated-stator current. Supplementary and stator copper losses are determined in this test. The total loss is determined as depicted in Tables 6.11 and 6.12.

Table 6.11. Loss in the radiator

Symbol	Quantity	Unit	Value
Q	Flow in the radiator	m <sup>3</sup> /s	0.041902
$T_i$	Water input temperature	°C	25.451
$T_o$	Water output temperature	°C	33.363
$\Delta T$	Temperature difference	°C	7.911
$P_1$	Total loss in the radiator	kW	1379.354

Table 6.12. Loss in the surfaces

Symbol	Quantity	Unit	Value
$P_{21}$	Loss in the generator covering	kW	23.754
$P_{22}$	Loss in the generator walls	kW	8.848
$P_{23}$	Loss in the turbine covering	kW	10.456
$P_2$	Total loss in the surfaces	kW	43.058

The ambient quantities observed during this test are depicted in table 6.13.

Table 6.13. Ambient quantities

Symbol	Quantity	Unit	Value
$P_{atm}$	Atmospheric pressure	mbar	936.67
UR	Relative humidity	%	34.33
$T_{amb}$	Temperature	°C	37.845
$\rho_{b0}$	Air density	kg/m <sup>3</sup>	1.134

The resulting ventilation loss here is **710.58 kW**. This value maintains itself almost constantly as described above. The armature copper loss and the rotor copper loss are **355.93 kW** and **85.94 kW** respectively. Therefore, the remaining loss regards the supplementary loss, which is **269.96 kW**.

### 6.2.2 Tests at full load

After developing tests under the three specified conditions that aim at determining the losses of the generator, a test at full load is applied. The test is conducted at the approximated rated conditions of 160 MVA and 0.95 power factor. The involved losses are presented in Table 6.14 whereas the ambient quantities observed during the development of this test are depicted in table 6.15.

Table 6.14. Full load losses

Symbol	Quantity	Unit	Value
$P_W$	Windage loss	kW	713.78
$P_C$	Core loss	kW	540.38
$P_{SC}$	Stator copper loss	kW	327.05
$P_S$	Stray-load loss	kW	237.69
$P_{RC}$	Rotor copper loss	kW	477.81
$P_{br}$	Brush losses	kW	5.93
$P_B$	Bearing friction loss	kW	156.17
$P_E$	Excitation loss	kW	33.96
$P_l$	Summation of losses	kW	2492.75
$P_o$	Power output	kW	154608.
$\eta_G$	Efficiency	%	98.41%

Table 6.15. Ambient quantities

Symbol	Quantity	Unit	Value
$P_{atm}$	Atmospheric pressure	mbar	940.89
UR	Relative humidity	%	30.10
$T_{amb}$	Temperature	°C	37.864
$\rho_{b0}$	Air density	kg/m <sup>3</sup>	1.134

The bearing losses were calculated using the thermodynamic method. The main measures are depicted in Table 6.16.

Table 6.16. Quantities for the bearing loss calculation

Symbol	Quantity	Unit	Value
Q	Flow in the bearing	m <sup>3</sup> /s	0.032103
T <sub>i</sub>	Water input temperature	°C	24.122
T <sub>o</sub>	Water output temperature	°C	26.667
ΔT	Temperature difference	°C	2.546
P <sub>B</sub>	Bearing loss (generator part)	kW	156.17

### 6.2.3 No-load saturation function test

The no-load saturation test was applied to the machine under a test that showed the results in Table 6.17, which depicts the excitation current and the related phase induced voltage.

Table 6.17. Results obtained in the no-load saturation test.

I <sub>F</sub> (A)	E (V)
0	0
87	1313
177	2624
266	3888
366	5212
471	6471
599	7805
646	8220
700	8646
757	9058
837	9566
916	9960
1022	10409
1155	10830
1335	11258

The same methodology presented in [6.2] is applied to these data, resulting in the contents of Table 6.18.

Table 6.18. Characteristics of the no-load saturation data

a <sub>v</sub>	20.37
b <sub>v</sub>	14.61
ΔI <sub>F</sub>	1.39

This indicates that a value of **1.39** must be added to the field current in order to have the airgap characteristic line passing through the origin. The inclination of the airgap line is **14.61**.

The rated field current is that which gives the rated phase voltage in the airgap. As the phase-to-phase rated voltage is 15000 V, the phase voltage is 8660 V, resulting in the rated field current of **592.7 A**.

A regression of a fourth order polynomial over the per-unit saturated voltage results in the following coefficients depicted in Table 6.19 and in the complete per-unit saturation curve of Fig. 6.5.

Table 6.19. Coefficients of the per-unit no-load saturation function

Coefficient	Value
$b_4$	7.4417
$b_3$	-22.228
$b_2$	24.85
$b_1$	-10.959
$b_0$	2.0737

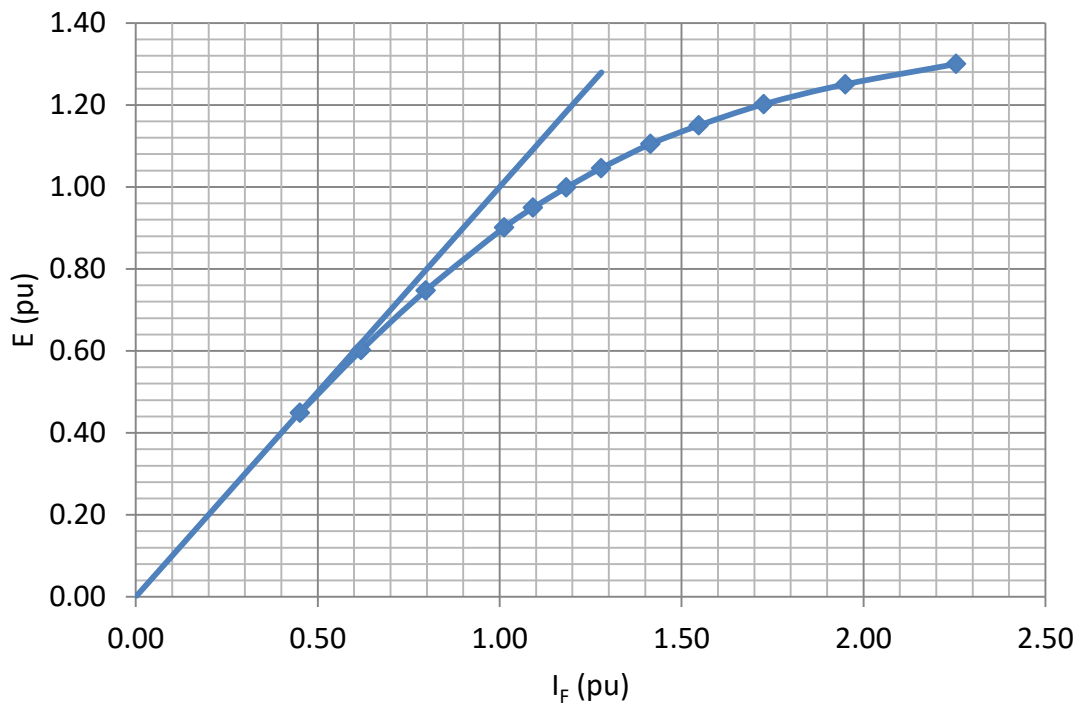


Figure 6.5. Complete per-unit saturation curve.

#### 6.2.4 Losses and efficiency calculation for any load

Once segregating the losses for the rated condition is done, the losses in other conditions can be calculated. The variation of the losses generally depends on the current squared. This can be seen, for example, both in the armature and in the rotor. Nevertheless, other losses also vary with the square of the current, such as the stray load loss and the loss in the brushes. The excitation power, on the other hand, is proportional to the field current, and the core loss is proportional to the square of the armature voltage.

As long as the armature current is directly proportional to the power output, the field current must be calculated for each operating point as previously described. For this generator with a  $X_d=0.8$  pu,  $X_q=0.6$  pu, and  $X_p=0.18$  and the application of the aforementioned equations, the family of V curves depicted in Fig. 6.6 can be obtained.

The V curves are a family of curves that relates the armature current with the field current for several active powers, depicting all of the operation points in a synchronous machine.

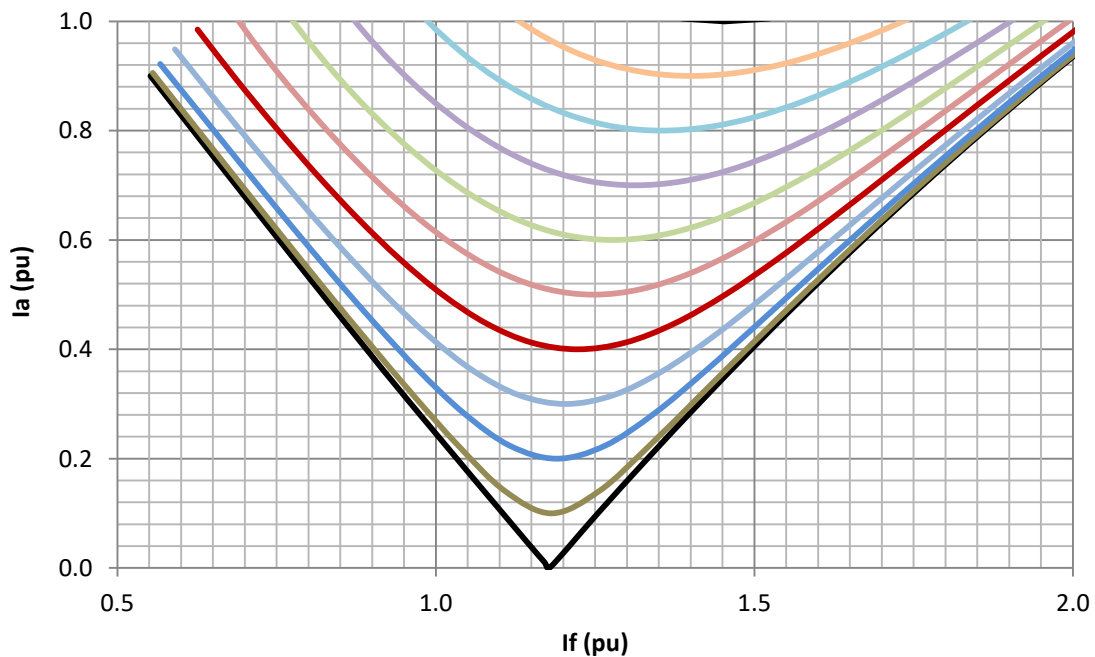


Figure 6.6. V-curve family for the machine under test.

With such values in hand, it is possible to obtain the map of efficiency of the machine under study, which is the variation of efficiency in the active and reactive power plane. Fig. 6.7 presents these results limited to the capability chart of the machine. While the map of efficiencies has no regard for whether the machine working in these such several points is possible or not.

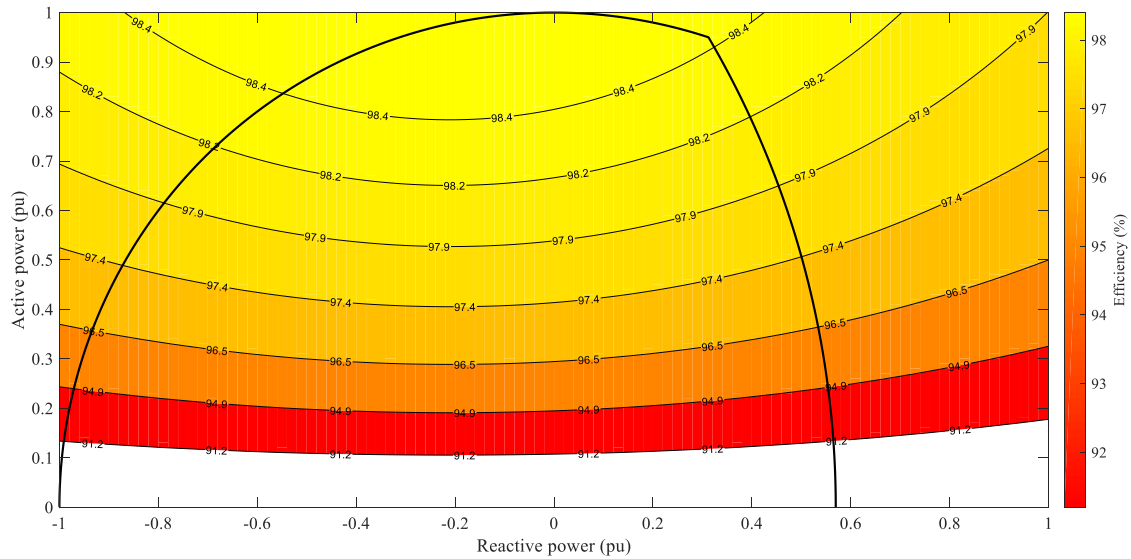


Figure 6.7. Map of efficiency of the tested machine limited by its capability chart.

The machine loading cycle of operation in the year 2017 was studied and presented in Fig. 6.8. For an expressive amount of the time, the machine was turned off, i.e., about 20% of a given year as shown in Fig. 6.9. When turned on, the machine assumes either very low active power or active powers between 0.6 and 0.95 per unit. On the other hand, the machine assumes a wide range of variation of reactive powers, mainly absorbing reactive power from the system, acting as a real synchronous condenser as shown in Fig. 6.9.

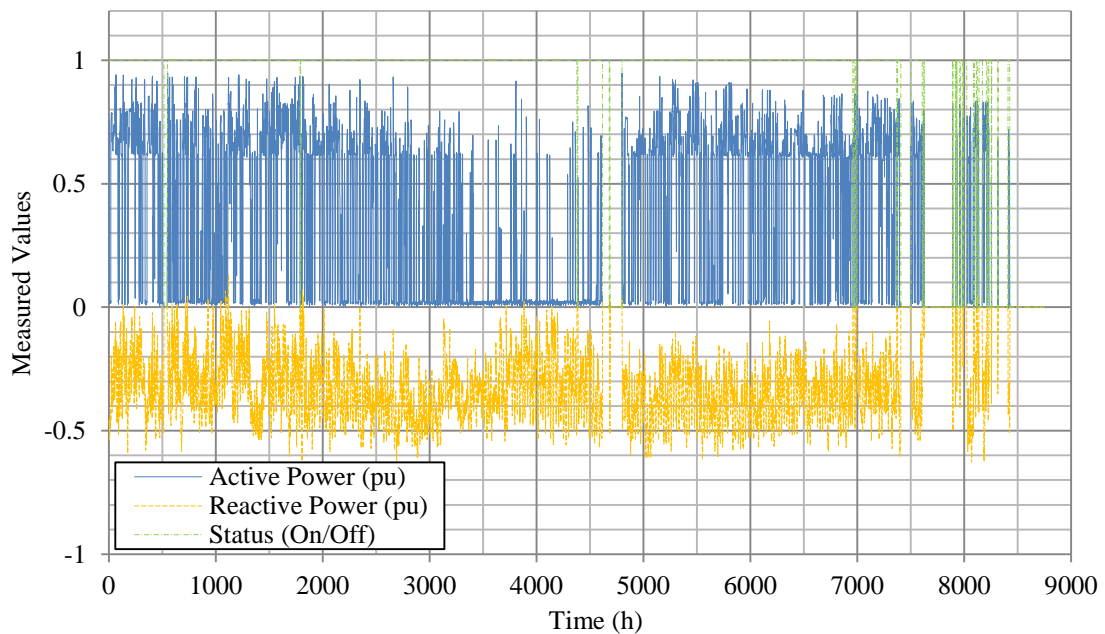


Figure 6.8. Loading in 2017.

Figure 6.10 presents a two-dimensional histogram (2D-Histogram) of the machine while operating. The color bar scale is in percentage of occurrence, showing the percentage of time operation during a given loading. The capability curve is also shown and presents the limits of the operation of this machine. It can be noted that some of the operating active and reactive power is beyond the limits of the capability chart.

It can be noticed that the machine has an efficiency of 98.5% in rated condition, i.e., an active power of 0.95 pu with a reactive power of 0.31 pu. On the other hand, a greater percentage of time, i.e., about 35% of time, it works at 0.65 pu of active power and -0.45 pu of reactive power. Additionally, it works in vicinities with an efficiency of about 96%. More detail of the picture in the high-active power range is shown in Fig. 6.11, where a point beyond the capability's limits can be observed.

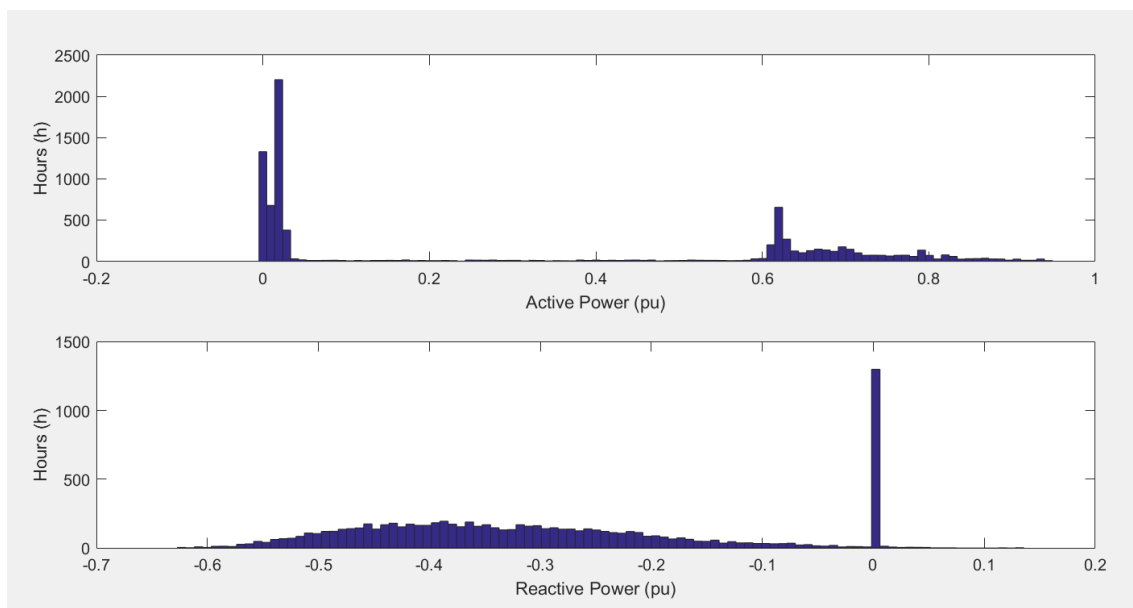


Figure 6.9. Histogram of loading in 2018

It can be observed that the machine does not work at its rated point in which the rated efficiency was established. Of course, the highest efficiency in rated point, or the highest efficiency out of this point, will work even though it is expected that the working efficiency ought to be less than the expected efficiency for the rated point.

The overall weighted average will be reached by evaluating the efficiency at a given loading point weighted by the number of hours of operation of the machine at this point or, in other words, with the probability to find the machine operating at this point.

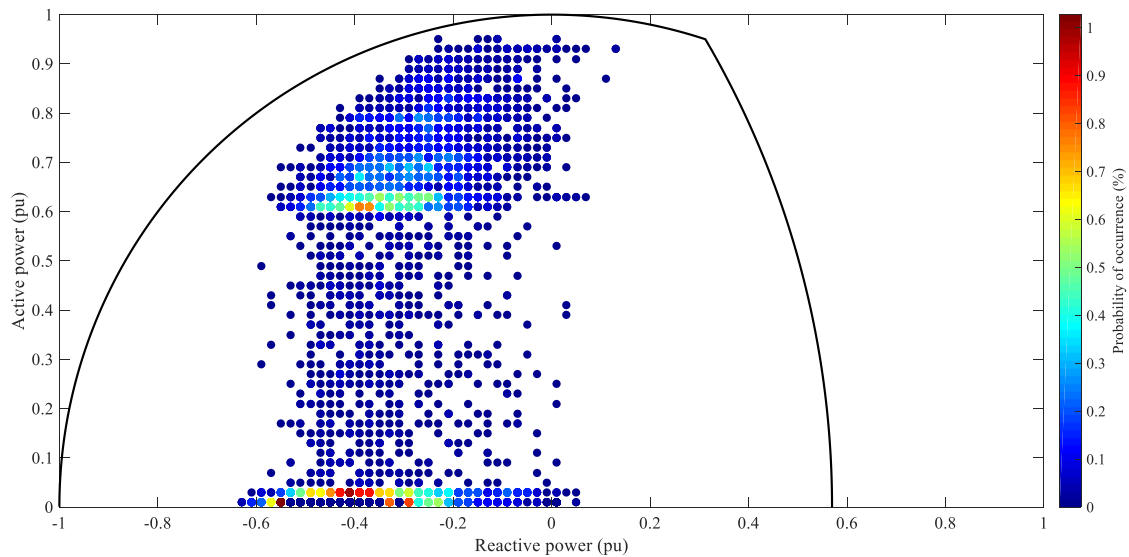


Figure 6.10. 2D-Histogram of the loading in 2017 in the P-Q plane.

The calculated overall average efficiency weighted by the time of operation is as low as **64.39%**. This low-weighted average efficiency arises because of the long duration of operation at low active power. If an active power equal to or greater than **0.60** is considered, the weighted average efficiency would be **98.00%**, which is still less than the efficiency at the rated loading of **98.35%**. This fact reinforces the importance of evaluating the weighted average efficiency rather than a single efficiency value.

## CAPÍTULO 7

### CONCLUSIONS

This study presented a proposal of not only supplying the efficiency at the rated point, but also one that considers the most probable loading points and in doing so evaluates the weighted average efficiency. A histogram of operation must be constructed for an existent generator and for newly-constructed generators, an estimate of the loading points and the percentage of time by which each one must be evaluated.

The main reasons of operating at a point different than the rated one are shown. This includes the input availability as well as the energy market. Therefore, the operational factor must be taken into account instead of considering the efficiency at a single point, but rather throughout all of the operational area.

A machine can be designed for a specific application. It was observed that the larger the diameter of a machine, the larger the losses will be. In addition, after several simulations, it was observed that the losses that really change the loading that occur the maximum efficiency are the stator current losses and the stray-load losses, which vary with the square of the stator current.

The analysis of an existing machine starts with the measurement of the efficiency at the rated point along with the segregated losses. This study presented an infrared based thermodynamic approach. Three different runs, all of which at special loading conditions, are necessary in order to obtain the segregate losses. After obtaining the losses at rated loading, the losses at any loading are estimated using procedures established in the main related standards.

Tests were conducted in an existent machine. The efficiency map was obtained and cross-referenced with the operational 2D-histogram. The average efficiency weighted by the time of operation in each loading point was thereby determined.

## BIBLIOGRAPHICAL REFERENCES

### Chapter 1 - Introduction

- [1.1] REN21, "Renewables 2017 - Global Status Report," 2017.
- [1.2] MME, "Ministério de Minas e Energia. Boletim mensal de monitoramento do setor elétrico - dezembro de 2016.," 2017.
- [1.3] GWEC, "Global Wind Statistics 2017," Global Wind Energy Council, Brussels, Belgium, Feb. 2018.
- [1.4] REN21, "Renewables 2018 Global Status Report," Renewable Energy Policy Network for the 21st Century, Paris, France, 2018.
- [1.5] DOE, "2017 Wind Technologies Market Report," U.S. Department of Energy, Alexandria, United States, 2018.
- [1.6] DOE, "2017 Offshore Wind Technologies Market Update," U.S. Department of Energy, Alexandria, United States, Sept. 2018.
- [1.7] IEA, "Technology Roadmap Wind Energy," International Energy Agency, Paris, France, 2013.
- [1.8] H. Polinder, S. W. H. Haan, M. R. Dubois, J. G. Sloopweg, "Basic Operation Principles and Electrical Conversion Systems of Wind Turbines," European Power Electronics and Drives, Vol. 15, pp. 43-50, Sept 2015.
- [1.9] Raihan, "Impact of Energy Storage Devices on Reliability of Distribution System," 2nd International Conference on Electrical, Computer & Telecommunication Engineering (ICECTE), 2016.
- [1.10] F. A. Farret, "Integration of Alternative Sources of Energy," John Wiley & Sons, pp. 262-295, 2017.
- [1.11] Akhil, G. Huff, A. B. Currier, B. C. Kuan, D. M. Rastler, S. B. Chen, A. L. Cotter, D. T. Bradshaw e W. D. Gauntlett, "DOE/EPRI 2013 Electricity Storage Handbook in Collaboration with NRECA," p. 163, 2013.
- [1.12] EPRI - Electric Power Research, "Electricity Energy storage Technology Options: A white paper Primer on Applications, Costs, and Bnefits.," EPRI, Palo Alto, CA, 2010.

### Chapter 2 - The weighted average efficiency concept

- [2.1] J. J. Roberts, A. M. Cassula, J. L. Silveira, E. C. Bortoni, A. Z. Mendiburud. Robust multi-objective optimization of a renewable based hybrid power system. Applied Energy 223 (2018) 52-68.
- [2.2] Z. Souza, A. H. M. Santos, E. C. Bortoni. Hydropower Plants – Implantation and commissioning (in Portuguese). Interciencia Editions. Rio de Janeiro, 522 p., 2018.
- [2.3] E. C. Bortoni, Z. Souza, A. N. C. Viana, H. F. Villa-Nova, A. J. J. Rezek, L. Lopes, R. T. Siniscalchi, R. A. Bragança, J. V. Bernardes Jr. Evaluation of the benefits of variable speed

operation of existent hydropower plants driven by Francis turbine. To appear in the Renewable & Sustainable Energy Reviews.

- [2.4] E C. Bortoni, G. S. Bastos, T. M. Abreu, B. Kawkabani. Online optimal power distribution between units of a hydro power plant. *Renewable Energy* 75 (2015) 30-36.
- [2.5] W. B. Esson. Notes on the design of multipolar dynamos. *Journal of the Institution of Electrical Engineers*, Vol. 20, Issue 93, May 1891, pp. 265-289.
- [2.6] J. E. Vrancik. Prediction of windage power loss in alternators. National Aeronautics and space administration. NASA TN D-4849. Lewis Research Center. Cleveland-OH, Oct. 1968.
- [2.7] IEC 60034-33 ED1 Rotating electrical machines - Part 33: Specific technical requirements for synchronous hydrogenerators including motor-generators. International Electrotechnical Commission, Geneve, 2019.
- [2.8] IEEE STD C50.12. IEEE Standard for 50 Hz and 60 Hz Synchronous Generators and Generator/Motors Coupled to Hydraulic Turbines and Rated 5 MVA and Above, 2019.
- [2.9] IEEE STD C50.13. IEEE Standard for Cylindrical-Rotor 50 and 60 Hz Synchronous Generators Rated 10 MVA and Above, IEEE standard C50.13-2005.
- [2.10] A. Joswig, M. Baca. Extended requirements on turbo-generators and solutions for flexible load operation. 2016 XXII International Conference on Electrical Machines (ICEM), 4-7 Sept. 2016, Lausanne, Switzerland.
- [2.11] Electrical Machinery Committee Task Force on Grid Code Impacts on Generator Standards. Consequences of Diverse Grid Code Requirements on Synchronous Machine Design and Standards. IEEE PES, 2018.
- [2.12] A. Joswig, H. Steins, J. R. Weidner, Impact of new flexible load operation and grid codes on turbine generators with a focus on end windings, presented on Power Gen Europe, 2015.

### Chapter 3 - Machine losses and efficiency

- [3.1] IEEE STD 115. IEEE Guide Test Procedures for Synchronous Machines, IEEE Standard 115-1995, Aug. 1995.
- [3.2] IEC 34-2, Rotating electrical machines. Part 2: Methods for determining losses and efficiency of rotating electrical machinery from tests (excluding machines for traction vehicles) Measurement of losses by the calorimetric method. Publication 34-2A, First edition, 1974)
- [3.3] IEC 60034-33; Rotating electrical machines – Part 33: Specific technical requirements for synchronous hydrogenerators including motor-generators. International Electrotechnical Commission, Geneve, 2019.
- [3.4] E. C. Bortoni, P. V. V. Silva, G. A. Braulio, R. T. Siniscalchi. Geometric Characteristics of Saturation Tests in Synchronous Machines. IEEE PES General Meeting. Atlanta, USA, 2019.

## Chapter 4 - Infrared based calorimetric method

- [4.1] IEEE STD 115. IEEE Guide Test Procedures for Synchronous Machines, IEEE Standard 115-1995, Aug. 1995.
- [4.2] IEC 34-2, Rotating electrical machines. Part 2: Methods for determining losses and efficiency of rotating electrical machinery from tests (excluding machines for traction vehicles) Measurement of losses by the calorimetric method. Publication 34-2A, First edition, 1974)
- [4.3] K. J. Bradley, W. Cao, J. Arellano-Padilla. Evaluation of stray load loss in induction motors with a comparison of input–output and calorimetric methods. IEEE Trans. on Energy Conversion, Vol. 21(3), Sep 2006, pp 682-689.
- [4.4] B. Szabados, A. Mihalcea. Design and implementation of a calorimetric measurement facility for determining losses in electrical machines. IEEE Trans. on Instrumentation and Measurement, Vol 51(5), Oct 2002, pp 902-907.
- [4.5] V. C. Silva, G. Meunier, A. Foggia, A 3D finite-element computation of eddy currents and losses in the stator end laminations of large synchronous machines. IEEE Trans. on Magnetics, Vol. 12(3), May 1996, pp 1569-1572
- [4.6] St. Kunckel, G. Klaus and M. Liese. Calculation of eddy current losses and temperature rises at the stator end portion of hydro generators. The International Journal for Computation and Mathematics in Electrical and Electronic Engineering, Vol. 22(4), 2003, pp. 877-890.
- [4.7] O. Aglén, A. Andersson. Thermal analysis of a high-speed generator. 38th IEEE IAS Annual Meeting Industry Applications Conference, Vol.1, Oct 2003, pp 547- 554.
- [4.8] L. R. Dupre, J. A. A. Melkebeek, R. Van Keer. On a numerical method for the evaluation of electromagnetic losses in electrical machinery. Int. Journal for Numerical Methods in Engineering, Vol. 39, 1996, pp 1535-1553.
- [4.9] S. Bogdanovic, D. Novac, I. Bleier, V. Milosavljevic, V. Vidakovic. Comparison of generator efficiency by measuring losses in cooling air and in cooling water. Proceedings of Power Systems Conference PSC 03, Timisoara, Romania, 2003.
- [4.10] D. Zlatanovici, R. Zlatanovici, D. Novac, M. Regli, S. Bogdanovici, Efficiency measurement by applying two different methods at the modernized hydrogenerators in Iron Gates I Hydroelectric power plant. Proceedings of the CIGRÉ, Paris, 2006.
- [4.11] W. Braga. Heat transmission. Thompson Learning, 2004.
- [4.12] F. Incropera. Fundamentals of heat and mass transfer, 6th Edition. Wiley. 2006.
- [4.13] H. Kaplan. Practical applications of infrared thermal sensing and imaging equipment. Third E. Spie Press. 2007.
- [4.14] S. Seghir-Ouali, D. Saurya, S. Harmand, O. Phillipart, D. Laloyb, Convective heat transfer inside a rotating cylinder with an axial air flow. International Journal of Thermal Sciences 45 (2006) 1166–1178.
- [4.15] E. C. Bortoni, R. T. Siniscalchi, J. A. Jardini. Determination of Hydro Generator Efficiency Using Infrared Thermal Imaging Techniques. IEEE Transactions on Energy Conversion, Vol 26(4), Dec. 2011, pp. 1134-1139.
- [4.16] E. C. Bortoni, R. T. Siniscalchi. Hydro generators losses measurement in accordance to IEEE-STD-115 and IEC-60034-2. 2012 IEEE Power and Energy Society General Meeting, San Diego, CA, USA.

## Chapter 5 - Capability chart of a generator

- [5.1] J. H. Walker. Operating characteristics of salient-pole machines. Journal of the Institution of Electrical Engineers, Vol 100, 1953, pp. 13-24.
- [5.2] R. M. Gove. Geometric construction of the stability limits of synchronous machines. Proc. IEE, Vol. 112(5), 1965, pp. 977-985.
- [5.3] M.M. Adibi, D. P. Milanicz. Reactive capability limitation of synchronous machines. IEEE Trans on Power Systems, Vol 9(1), 1994, pp. 29-40.
- [5.4] CIGRÉ. Generator On-Line Over and Under Excitation Issues Working Group A1.38. June 2015.
- [5.5] P. Costa Jr., A. N. Souza, P. S. Silva, J. E. C. Castanho. A Visual Tool for Building Synchronous Generator Capability Curves. Proceedings of IEEE Southeastcon, Jacksonville, 2013.
- [5.6] A. Losi, M. Russo, P. Verde, D. Menniti. Capability chart for generator-transformer units. IEEE Trans on Energy Conversion, Vol 13(1), 1988, pp. 90-95.
- [5.7] G. Valverde, J. J. Orozco. Reactive Power Limits in Distributed Generators from Generic Capability Curves. IEEE PES General Meeting, National Harbor, 2014.
- [5.8] C. H. C. Guimarães, R. D. Rangel. Despacho de Unidades Geradoras Considerando os seus Limites de Capacidade. XI Symposium of Specialists in Electric Operational and Expansion Planning, Florianópolis. 2009.
- [5.9] L. Qiang, L. Yong-gang, L. Hai-bo. Steady-state stability limit of turbine-generators in consideration of AVR. Proceeding of International Conference on Electrical Machines and Systems, Seoul, Korea, 2007.
- [5.10] A. Capasso, E. Mariam. Influence of Generator Capability Curves Representation on System Voltage and Reactive Power Control Studies. IEEE Trans PAS, Vol 97(4), 1978, pp. 1036-1041.
- [5.11] X. M. Jia and S. S. Choi. Design of Volts per Hertz Limiter with Consideration of the Under-Excitation Limiter Control Actions. IEEE Trans on Energy Conversion, Vol. 16(2), 2001, pp. 140-147.
- [5.12] Charles J. Mozina, M. Reichard. Coordination of generator protection with generator excitation control and generator capability. WG J-5 of the Rotating Machinery Subcommittee, Power System Relay Committee.
- [5.13] A. Murdoch, G.E. Boukarim, M.J. D'Antonio and R.A. Lawson. Generator Over Excitation Capability and Excitation System Limiters. IEEE Power Engineering Society Winter Meeting. Columbus, 2001.
- [5.14] C. H. C. Guimarães, R. D. Rangel. Diagramas operacionais de unidades geradoras. X Symposium of specialists in electric operational and expansion planning. Florianópolis, 2006.
- [5.15] J. P. Hunt. Capability curves and excitation requirements of saturated cylindrical rotor synchronous machines. IEEE Trans on PAS, Vol. 86(7), 1967, pp. 855-859.
- [5.16] N. E. Nilsson, J. Mercurio. Synchronous generator capability curve testing and evaluation. IEEE Transaction on Power Delivery, Vol. 9(1), 1994, pp. 414-424.

- [5.17] J.W. Feltes, S. Orero, B. Fardanesh, E. Uzunovic, S. Zelingher, N. Abi-Samra . Deriving Model Parameters from Field Test Measurements. IEEE Computer Applications in Power, Vol 15(4), 2014, pp. 30-36.
- [5.18] USBR. Permissible loading of generators and large motors. United States department of the interior bureau of reclamation, 1991.
- [5.19] J. C. Agee. Maximizing Benefits of Temporary Generator Overexcited Capability: A Special Technical Session on New Operating Concepts. 2001, pp. 203-204.
- [5.20] ANSI/IEEE C37.10b. IEEE Standard for Emergency Load Current-Carrying Capability. 1985.
- [5.21] V. F. Estcourt, C. H. Holley, W. R. Johnson, P. H. Light. Underexcited operation of large turbine generators on pacific gas and electric company's system. Trans of the AIEE. Part III: Power Apparatus and Systems. 72(1), 1953, pp. 16-22.
- [5.22] S. S. Choi, X. M. Jia. Under excitation limiter and its role in preventing excessive synchronous generator stator end-core heating. IEEE Trans on Power Systems, Vol 15(1), 2000, pp. 95-101.
- [5.23] S. B. Farnham, R. W. Swarthout. Field excitation in relation to machine and system operation. Trans of the AIEE. Part III: Power Apparatus and Systems, Vol 72(6), 1953, pp. 1215-1223.
- [5.24] J. H. Carter, R. E. Gorman. Operation of Large Steam Turbine Generators. Electrical Engineering, Vol 75(6), 1956, pp. 545 – 545.

## Chapter 6: Application to existent machine

- [6.1] EM.O, GES.O, DEAM.O. Efficiency test of generating unit 6 (UG#6) of Furnas Hydropower Plant – Results presentation. São José da Barra, 2015.
- [6.2] E. C. Bortoni, P. V. V. da Silva, G. A. Braulio, R. T. Siniscalchi, “Geometric Characteristics of Saturation Tests in Synchronous Machines” in Proc. IEEE PES General Meeting, Atlanta, GA, 2019.